On the use of vertically averaged models to simulate CO_2 migration in a layered saline aquifer

Master Thesis in Applied Mathematics and Computational Mathematics

Basil Fayez El-Faour

Department of Mathematics

University of Bergen

June 2010

Abstract

Geologic and flow characteristics such as permeability and porosity, capillary pressure, geologic structure, and thickness all influence and affect CO_2 plume distribution to varying degrees. These parameters do not necessarily act independently. Depending on the variations in these parameters one may dominate the shape and size of the plume [4].

In this master thesis, we consider the long-term fate and migration of a large CO_2 plume that takes place in a heterogeneous (two-layer) sloping saline aquifer.

We consider a vertical equilibrium (VE) mathematical model to study the effect of two different permeability layers on the shape, speed and migrated distance of the CO_2 plume. The layer-permeability-ratio is k_2/k_1, where $k_2 \ll k_1$ and k_2, k_1 are the permeabilities in the upper and lower layer of the aquifer, respectively. We also study the effect the thickness ratio of the lower permeability($h = \frac{1}{2}H$, $h = \frac{1}{4}H$, $h = \frac{1}{8}H$), where H is the thickness of the aquifer. We attain these goals by comparing the simulation results of Eclipse and VE simulators, where both simulate the movement of CO_2 plume in homogeneous and layered aquifers.

A VE model has been built considering one-dimensional flow in the x-direction, due to the big difference in scale length between vertical and horizontal directions. We model a 2D vertical section in Eclipse simulator, taking the vertically averaged of this section ends up with a 1D results that can compared with the VE solution.

Our results shows that the variations in the vertical permeability layers may have a dramatic effects on the CO_2 plume shape. Relatively lower permeability layer reduces the velocity of CO_2 through it, and an increase of CO_2 saturation occurs below this layer. At early time, the build up in saturation increases, and the lateral growth of the CO_2 immediately below this layer increases. At later time, the saturation decreases and the vertical flow of the CO_2 in this layer increases. The k_2/k_1 ratio and thickness of the lower per-

meability layer determines the plume shape and distance migrated. In some of our simulations, the results show two connected/disconnected plumes.

Preface

During the work on this thesis I have received valuable assistance and support from several people.

Firstly, I would like to thank my supervisors Helge Dahle and Jan Nordbotten who have guided me in the profession of mathematics and in the field of CO_2 research. They have also given me the opportunity to travel to distant places like Svalbard, Paris and London, something that is not very usual for a Palestinian refugee. For that I am very grateful.

Secondly, I would like to thank Paulo Herrera for his great help with the finalization of my thesis.

Thirdly, Meisam Ashraf has been of invaluable assistance in helping me to find out the secrets of Eclipse.

Fourthly, thanks to all my friends who have helped and supported me.

Finally, I would like to thank my family, wife Gunhild, mother Syria for being supportive all the time.

Outline

This master thesis consists of 6 chapters. In the first chapter we introduce the idea behind geological storage of CO_2 and we describe the main mechanisms that prevent CO_2 from leaking out of storage site and back to the atmosphere. In chapter 2 the basic physics of two-phase is given and flow properties and govering equations are introduced. Moreover, we introduce the vertically averaged equations used for a homogenous and a layered aquifer with N-layers. In chapter 3 we introduce the numerical methods that we use to discretize and solve our model. In chapter 4 we introduce two simulators which are used in this study: a simulator based on our own MATLAB implementation of the methods described in chapter 3. In addition we use the industry standard Eclipse simulator to represent a "full physics" model. Our simulation results are introduced in chapter 5. Finally, our conclusion and suggestions are introduced in chapter 6.

Contents

Chapter 1

Introduction

Increasing atmospheric concentrations of greenhouse gases, such as carbon dioxide (CO_2), are suspected to be the main cause of a gradual increase in global temperatures [17]. Capture and storage of CO_2 is considered as one of the most promising alternatives among possible mitigation actions to reduce greenhouse gas emissions. It is estimated that giga tones of CO_2 will have to be stored every year to make a significant contribution to the mitigation of climate change [18]. There are multiple alternatives for the storage of CO_2 including CO_2 injection into deep oceans, saline aquifers, unminable coal seams or depleted oil and gas reservoirs; in combination with the use of CO_2 in enhanced oil and coal bed methane recovery. However, storage in deep saline aquifers it appears to be the best choice in terms of resident storage time, storage capacity and proximity to emission sites [10].

1.1 Geological sequestration of CO_2 in saline aquifers

The term "saline aquifer" is used for deep sedimentary rocks saturated with water formation or brine (water with high contents of dissolved salts). This brine cannot be used as a source of drinking water or irrigation because of its' high salinity. Saline aquifers occur in all sedimentary basins and are not restricted to coal, oil, or gas provinces [10].

CO_2 is injected in a supercritical state to decrease the storage volume (one tonn of CO_2 that occupies a volume of 509 m^3 at standard conditions for temperature and pressure (STP), will occupy only 1 m^3 as supercritical fluid)

[13]. For CO_2 to be in the supercritical state the depth required is approximately 800 m for a typical geothermal gradient of $25\,^{\circ}\mathrm{C}\,\mathrm{km}^{-1}$ [10]. Although supercritical CO_2 is much denser than CO_2 in its' gaseous phase, it is less dense than brine under all continental and shallow marine storage conditions [10]. Because of the density difference, injected CO_2 moves upward in the vertical direction reaching the top cap rock and spreading along it. If the cap rock has some fractures, then the risk of CO_2 leakage takes place. For more details about CO_2 leakage estimation see [2].

The injection of CO_2 into a heterogeneous reservoir saturated in brine is a rich and complex problem. Heterogeneity plays an important role in preventing the CO_2 plume rising too quickly through the reservoir, and spreads out the plume laterally within the reservoir in successive layers. This has two important effects: i) it fills a large portion of a vertical column of the reservoir with CO_2, thus improving storage efficiency, and ii) it increases the interface area between CO_2 and water, thus enhancing CO_2 immobilization through dissolution and consequent mineral reactions [20].

1.2 CO_2 trapping mechanisms

Several trapping mechanisms (Figure 1.1) act to prevent the migration of the buoyant supercritical CO_2 back to the surface [1]:

1. Structural trapping: Once injected, buoyant CO_2 will migrate upwards through the porous rock until it reaches the impermeable cap rock.

2. Capillary or residual trapping: During injection, CO_2 displaces brine at the tip of the plume as it moves through the formation in a drainage process. After injection stops, brine displaces the CO_2 at the tail of the plume in an imbibition process, but some CO_2 is left behind as disconnected or residual trapped blubbles.

3. Dissolution or solubility trapping: Supercritical CO_2 dissolves in brine, forming a denser brine-CO_2 liquid mixture than the pure CO_2 or pure brine. This denser solution will sink to the bottom of the rock formation over time due to gravity.

4. Mineral trapping: This is the result of CO_2 dissolution in brine, where it forms a weak carbonic acid. Over time, this weak acid can react with the minerals in the surrounding rock to form solid carbonate minerals.

Trapping mechanisms take place over different time scales, from days to thousands of years. See Figure 1.2. In general, geologically stored CO_2 becomes more securely trapped with time [1].

Figure 1.1: Structural (top left), residual (middle left), dissolution (bottom left) and mineral (right) trapping. Taken from http://www.co2captureproject.org/co2_trapping.html. [1]

In this thesis, we are only interested in structural and residual trapping. These two trapping mechanisms are also considered to be more important in the first hundred years after injection.

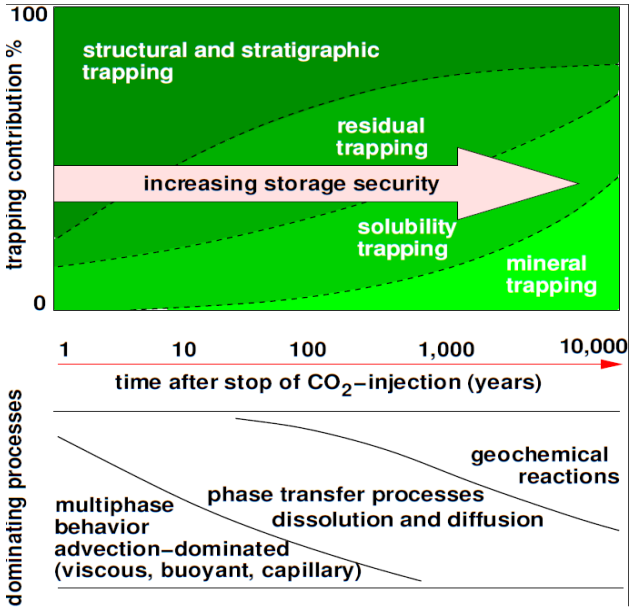

Figure 1.2: Storage security depending on different trapping mechanisms and dominant proccesses over time (modified after IPCC (2005), Class (2008).

In addition to the trapping mechanisms, we are also interested in the shape of the CO_2 plume in order to estimate effective storage volumes. The effect of the imperfect vertical sweep on the migration distance and time of the current have been considered in [10] . For the hyperbolic limit, they showed that in the presence of residual trapping, the current volume is reduced to zero in finite time, and their results suggest that the efficient residual trapping in dipping aquifers may result in CO_2 storage in aquifers lacking structural closure, if CO_2 is injected far enough from the outcrop of the aquifer.

Chapter 2

Mathematical model

In this chapter, a mathematical model for two phase flow in a reservoir is introduced. This chapter is divided into four parts. First, we introduce the main concepts related to multiphase flow in porous media. Second, we present the set of equations that define the model. Third, we set up our assumptions for simplifying the problem. Finally, we present the derivation of a vertically averaged model for the aquifer with two vertical layers, then we generalize those results for the case of an aquifer with N layers.

2.1 Multiphase flow in porous media

The general properties that characterizes the ability of a porous media to transport a fluid are **porosity** and **permeability**.

2.1.1 Porosity

The effective porosity, ϕ, of a porous medium is defined as the fraction of the total volume of the medium that is occupied by interconnected pores, or void space of interconnected pores [9], i.e.

$$\phi = \frac{V_{pores}}{V_{total}} \tag{2.1}$$

In addition to the connected pores, the pore space contains isolated pores that may not transport fluids, see Figure 2.1. Table 2.1 lists typical porosity values for rock reservoir [5].

if	$0 < \phi < 5\%$	$\Longrightarrow$	Negligible
if	$5 < \phi < 10\%$	$\Longrightarrow$	Poor
if	$10 < \phi < 15\%$	$\Longrightarrow$	Fair
if	$15 < \phi < 20\%$	$\Longrightarrow$	Good
if	$20 < \phi < 25\%$	$\Longrightarrow$	Very Good
if	$\phi > 25\%$	$\Longrightarrow$	Excellent

Table 2.1: Reservoir rock porosity [5]

Figure 2.1: Porous medium

2.1.2 Permeability

Permeability, $\underline{k}$, is defined as the ability of the rock to transmit (conduct) fluids in different directions, and it depends on the porosity of the rock. Thus, non-porous rocks have no permeability. If the rock transmits the same amount (volume) of a fluid in all directions, then isotropic permeability is defined, else anisotropic permeability is defined. Also the type of clay or cementing material between sand grains affects the permeability, especially where fresh water is present. Some fine grained material, such as clay swells in fresh water and has a tendency to partially or completely block the pore spaces.. Absolute permeability is the measurement of the permeability conducted when a single fluid, or phase, is present in the rock. Effective permeability is the ability to preferentially flow or transmit a particular fluid through a rock when other immiscible fluids are present in the reservoir (for example, effective permeability of gas in a gas-water reservoir). The permeability tensor, $\underline{k} = k\underline{I}$, is isotropic in the remaining of this thesis.

Permeability of petroleum reservoir rocks may range from 0.1 to 1000 or more millidarcies. The quality of the reservoir as determined by permeability, in

mD (1 mD= 10^{-3} Darcy, 1 Darcy $\simeq 0.987x10^{-12}$ m^2), may be judged as listed in Table 2.2 [5]:

if	$k <$ 1mD	$\Longrightarrow$	Poor
if	1mD $< k <$ 10 mD	$\Longrightarrow$	Fair
if	10mD $< k <$100 mD	$\Longrightarrow$	Good
if	100mD $< k <$ 1000 mD	$\Longrightarrow$	Very Good
if	$k >$1000 mD	$\Longrightarrow$	Excellent

Table 2.2: Reservoir rock permeability [5]

2.2 Governing equations

In this section we present the governing equations of immiscible and incompressible two-phase flow in a porous medium.

2.2.1 Two-phase flow

CO_2 migration in saline aquifers fully initialized with brine can be modeled as a two phase immiscible fluid system using the generalized Darcy's law. In a two-phase CO_2 and brine system, the CO_2 will be the non-wetting (nw) and brine the wetting (w) fluids.

The behavior of CO_2 and brine is governed by the mass balance equation for each phase, Darcy's law, relative permeability and capillary pressure.

2.2.2 Residual saturation

The saturation S_i, of phase i describes the volume fraction occupied by the phase i and the total volume in a given area. The void space is occupied by either CO_2, brine or both and the sum of the saturation's of the phases is equal to one.

$$S_{nw} + S_w = 1$$

Residual saturation $S_{r,i}$, is defined as the saturation level below which fluid drainage and imbibition will not occur, where $i = w$, nw.

2.2.3 Relative permeability

If some of the pore volume is occupied by one phase then there is less space for the other phase to flow in. Relative permeability is introduced to correct the reduction of pore space. The permeability describes how it effects the flow, while the relative permeability describes how the flow is effected when two or more phases interact with each other. The relative permeability is dependent on the saturation of the phases. The effective permeability of a fluid at a given saturation in the reservoir is the product of the permeability related to the rock and the relative permeability related to the phases. The relative permeability is typically specified as a function of reduced water saturation [25]

$$k_{r,i} = k_{r,i}(\hat{S}), \;\; i = w, \; nw$$

where $\hat{S}$ is the reduced water saturation defined as

$$\hat{S} = (S_w - S_{r,w}) \,/\, (1 - S_{r,w} - S_{r,nw}) \,.$$

In this expression S_w is the wetting saturation, and $S_{r,w}$, $S_{r,nw}$ are the irreducible wetting and non-wetting saturations, respectively.

2.2.4 Mass conservation

The principle of mass conservation establishes that the change of total mass inside a fixed (time independent) volume, must be balanced by the flux of mass over the boundary of that volume, and the contribution of sources or sinks inside the volume. Then, the mass conservation equation in terms of fluid saturation S_i can be written as,

$$\frac{\partial \left(\rho_i \phi S_i\right)}{\partial t} + \nabla \cdot \left(\rho_i \underline{u}_i\right) \;\; = \;\; \rho_i \psi_i \qquad i = nw, w \tag{2.2}$$

where $\underline{u}_i$ the volumetric flux vector is determined by the generalized Darcy's law, ϕ is the porosity and S_i, ρ_i, ψ_i are the saturation, density and source or sink of phase i respectively.

2.2.5 Darcy's law

Darcy's law is an empirical (*experimental*) law, which relates the applied forces (pressure gradients and gravity) to fluid flow in porous media. The generalized Darcy's law for two phases is written as

$$\underline{u}_i = -\frac{kk_{r,i}}{\mu_i}\left(\nabla p_i + \rho_i g e_z\right) \qquad i = nw, w \tag{2.3}$$

where k is the absolute rock permeability value, g the gravity acceleration, e_z the z-direction upward with respect to gravity and k_{ri}, p_i and μ_i are the relative permeability, pressure and viscosity of phase i respectively.

A complete 3D model equations for two-phase CO_2/brine system can be summarized as:

- Darcy's law:

$$\underline{u}_i = -k\lambda_i(\nabla p_i + \rho_i g e_z), \qquad \lambda_i = \frac{k_{r,i}}{\mu_i} \qquad i = nw, w$$

- Conservation equation:

$$\phi\frac{\partial}{\partial t}(S_i) + \nabla \cdot \underline{u}_i = 0$$

- Relative permeability

$$k_{r,i} = k_{r,i}(S_w)$$

- Viscosity:

$$\mu_i = \mu_i(p_i)$$

- Volume balance:

$$S_{nw} + S_w = 1$$

- Capillary pressure:

$$p_{nw} - p_w = p_c(S_w)$$

2.3 Assumptions

The 3D model above is expensive to solve, e.g., because of unstable flow and gravity override. Some assumptions are needed in order to get a closed model that is able to represent the most important physics in the reservoir and to ensure that there is no CO_2 leakage through the boundary cap rocks, such as

- Impermeable Boundaries: no flow at the top and bottom cap rocks boundaries of the reservoir, except at the upper right-hand edge and the left-hand edge " no-flow condition " i.e, $\underline{u}_i \cdot \underline{n} = 0, \quad \texttt{where } i = nw, w$
- Hydrostatic equilibrium: Horizontal velocity (parallel to the aquifer plane) $\gg$Vertically velocity (normal to the aquifer plane).
- Flow of two immiscible fluids.
- Incompressible fluids($\rho = \rho_{\texttt{initial}} = \texttt{constant}$).
- No source or sink terms (no dissolution).
- Constant porosity($\phi = 15\%$).
- No capillary pressure ($p_c = 0$; Sharp-interface).

2.4 Vertically averaged equations

Because the vertical length scale is much smaller than the horizontal length scale in the above full three-dimensional model, vertically averaged equations are introduced to reduce the number of calculations needed. We ends up with a full model in two-dimensions upon averaging in the vertical direction. For further simplification, we solve this vertical model in x-direction only.

2.4.1 Non-layered aquifer(n=1)

Following Nordbotten and Dahle [24], we consider the flow of supercritical CO_2 with density $\rho_c = \rho$ and of brine with density $\rho_b = \rho + \Delta\rho$ in a sloping aquifer as shown in Figure 2.2. The CO_2 height is given by $h_c(x, y) = H - h$, while brine height is $h_b(x, y) = h$.

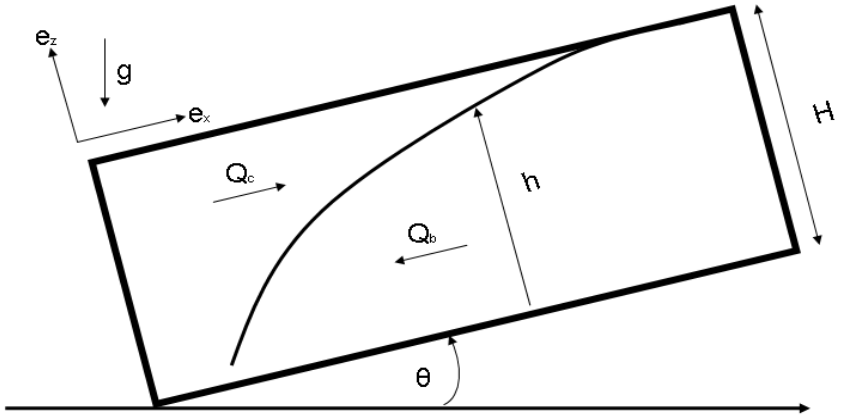

Figure 2.2: Flow direction of CO_2 and brine, and the 2D Cartesian coordinate system(e_x, e_z) considered. In this coordinate system $\underline{g} = -g\sin(\theta)e_x - g\cos(\theta)e_z$.

Assuming hydrostatic equilibrium, the pressure inside the aquifer is given by

$$p_i = p_{\texttt{bottom}} - \rho_i g cos(\theta) z \tag{2.4}$$

where p_{bottom} is the pressure at the lower aquifer plane and z is the position or coordinate of the point where we are measuring the pressure.

Defining the vertically averaged parameters

$$\overline{\phi} = \frac{1}{H}\int_0^H \phi dz \tag{2.5}$$

$$\overline{k} = \frac{1}{H}\int_0^H k dz \tag{2.6}$$

$$\overline{S_i} = \frac{1}{\overline{\phi} H}\int_0^H \phi S_i dz \tag{2.7}$$

$$\overline{\underline{u}} = \frac{1}{H}\int_0^H \underline{u_i} dz \tag{2.8}$$

$$\overline{k}_{r,i} = \frac{1}{\overline{k}H}\int_0^H k k_{r,i} dz \qquad \overline{\lambda}_i = \frac{\overline{k}_{r,i}}{\mu_i} \tag{2.9}$$

$$\overline{q}_i = \frac{1}{H}\int_0^H q_i dz \tag{2.10}$$

where $\underline{u}_i$ is the velocity in the $x-y$ direction, $\overline{\phi}$, $\overline{k}$, $\overline{S_i}$, $\underline{\overline{u}}$, $\overline{k}_{r,i}$, $\overline{\lambda}_i$ and $\overline{q}_i$ are the vertically averaged porosity, permeability, saturation, velocity, relative permeability, mobility and source (sink) respectively.

Noting that the averaged relative permeability and mobility are functions of the averaged saturation, i.e.

$$\overline{k}_{r,i} = \overline{k}_{r,i}(\overline{S}_n) \qquad \overline{\lambda}_i = \overline{\lambda}_i(\overline{S}_{nw}) \tag{2.11}$$

Thus, the full 2D model equations for two-phase CO_2/brine system obtained

$$\frac{\partial}{\partial t}(\overline{\phi}\,\overline{S}_i) + \nabla_{\parallel}\underline{\overline{u}}_i = \overline{q}_i \tag{2.12}$$

$$\underline{\overline{u}}_i = -\overline{\lambda}_i\overline{k}[\nabla_{\parallel}p_i + \rho_i g\sin(\theta)e_x] \tag{2.13}$$

$$\overline{S}_{nw} + \overline{S}_w = 1 \tag{2.14}$$

$$\overline{k}_{r,i} = \overline{k}_{r,i}(\overline{S}_w) \tag{2.15}$$

$$\overline{\lambda}_i = \overline{\lambda}_i(\overline{S}_w) \tag{2.16}$$

with $\nabla_{\parallel} = (\frac{\partial}{\partial x}, \frac{\partial}{\partial y})$.

To simplify more, we assume fluid flow in the x-direction (one-dimensional flow) only.

2.4.2 Sharp-interface approximation

A sharp interface approximation assumes that the saturation of the non-wetting phase is either S_{nwr} or $1 - S_{wr}$ without intermediate values, which is equivalent to neglect the capillary transition zone. Then

$$S_{nw} = \begin{cases} S_{r,nw} & 0 \leq z < h, \\ 1 - S_{r,w} & h < z \leq H, \end{cases} \tag{2.17}$$

where $z = h$ is the unknown location of the interface.

We have that $\nabla \overline{p}_c = \nabla[p_c - \Delta\rho g \cos(\theta) z]$, where p_c is the fine scale capillary pressure which is equal to zero in our reference case. If porosity and permeability are isotropic and independent of z, then

$$\overline{S}_{nw} = \frac{h}{H} S_{nwr} + (\frac{H-h}{H})(1 - S_{r,w}) \tag{2.18}$$

$$\overline{\lambda}_{nw}(\overline{S}_{nw}) = \lambda_{r,nw}(\frac{H-h}{H}) \tag{2.19}$$

$$\overline{\lambda}_{w}(\overline{S}_{nw}) = \lambda_{r,w}(\frac{h}{H}) \tag{2.20}$$

where $\lambda_{r,nw} = \frac{k_{r,nw}(S_n = 1 - S_{r,w})}{\mu_n}$ and $\lambda_{r,w} = \frac{k_{rw}(S_{r,nw})}{\mu_w}$ are the mobilities of the non-wetting and wetting phases shown in Figure 2.3 B. If residual trapping is considered (see Figure 2.3 B), then we have that

$$S_{nw} = \begin{cases} 0 & 0 \leq z < h_{min} \\ S_{r,nw} & h_{min} < z \leq h \\ 1 - S_{r,w} & h < z \leq H \end{cases} \tag{2.21}$$

where $h_{min} \leq h$. From Figure 2.3 B we observe that

- $\frac{\partial h}{\partial t} > 0 \Rightarrow h_{min} < h$ (Drainage, then h increasing upward).
- $h_{min} \neq h \Rightarrow \frac{\partial h_{min}}{\partial t} = 0$.

In this case the averaged saturation and mobility relationships become

$$\overline{S}_{nw} = \frac{(h - h_{min})}{H} S_{r,nw} + (\frac{H-h}{H})(1 - S_{r,w}) \tag{2.22}$$

$$\overline{\lambda}_w(\overline{S}_{nw}) = \lambda_{wo}\frac{h}{H} + (\lambda_{r,w} - \lambda_{wo})(\frac{h - h_{min}}{H}) \tag{2.23}$$

where $\lambda_{wo} = \frac{k_{r,w}(S_{r,nw}=0)}{\mu_w}$, shown in Figure 2.3 B. Note that $\overline{\lambda}_{nw}(\overline{S}_{nw})$ did not change with respect to equation (2.19).

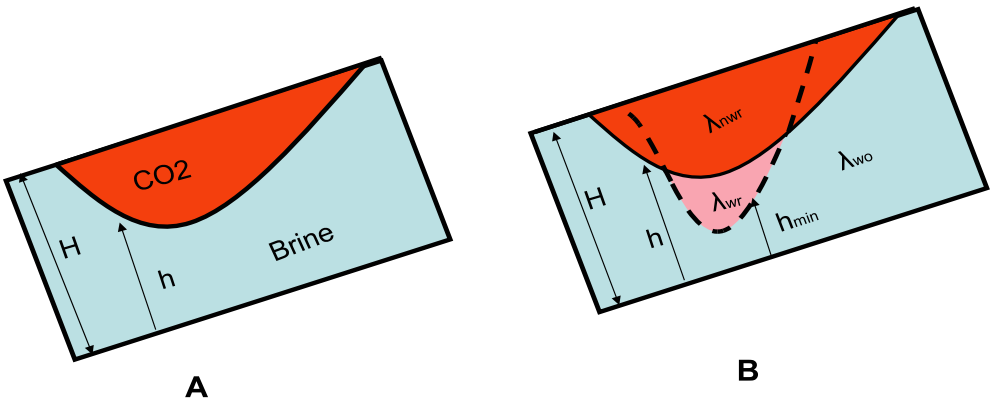

Figure 2.3: Schematic of sharp interface approximation without residual trapping (A) and with residual trapping (B).

Referring to our reference case where no source or sink exists and the mean flow flows in the x-direction, then $\overline{u}_{total} = 0$, $\overline{q}_i = 0$, $z = h$ and $\nabla_{\parallel} \equiv \frac{\partial}{\partial x}$. The expression of the averaged saturation equation can be produced by subistituting equation (2.23) in (2.13), then we subistitute the resulting equation and (2.22) in (2.12), such as

$$\frac{\partial h}{\partial t} + \kappa\frac{\partial}{\partial x}\left\{\frac{(h-H)\left[h + \delta\lambda_w\left(h_{min} - h\right)\right]}{(1-M)\,h + MH + \delta\lambda_w\left(h_{min} - h\right)}\left(sin\left(\theta\right) + cos\left(\theta\right)\frac{\partial h}{\partial x}\right)\right\} = 0 \tag{2.24}$$

where

$$\kappa = \begin{cases} \frac{\lambda_{r,nw}k\Delta\rho g}{\phi(1-S_{r,w})} & h = h_{min} \quad \texttt{Drainage} \\ \frac{\lambda_{r,nw}k\Delta\rho g}{\phi(1-S_{r,w}-S_{r,nw})} & h \neq h_{min} \quad \texttt{Imbibition} \end{cases} \tag{2.25}$$

$\delta\lambda_w = \frac{\lambda_{r,w}(S_{nw}=0) - \lambda_{r,w}(S_{nw})}{\lambda_{r,w}(0)}$ and $M = \frac{\lambda_{r,nw}}{\lambda_{wo}}$.

2.4.3 Layered aquifer (n≥2)

In this section we will present the vertically averaged equations for permeability, relative permeability and porosity assuming an aquifer with layered permeability.

Assuming an aquifer with two permeability layers (Figure 2.4 A) , the vertically averaged porosity, permeability, and relative permeability for the first layer are given by

$$\overline{\phi}_1 = \frac{1}{h_1}\int_0^{h_1} \phi_1 dz; \;\; \overline{k}_1 = \frac{1}{h_1}\int_0^{h_1} k_1 dz \tag{2.26}$$

$$\overline{k}_{r,nw1} = \frac{1}{\overline{k}_1}\frac{1}{h_1}\int_0^{h_1} k_1 k_{r,nw} dz \tag{2.27}$$

$$\overline{k}_{r,w1} = \frac{1}{\overline{k}_1}\frac{1}{h_1}\int_0^{h_1} k_1 k_{r,w} dz \tag{2.28}$$

and for the second layer

$$\overline{\phi}_2 = \frac{1}{(h_2 - h_1)}\int_{h_1}^{h_2} \phi_2 dz; \;\; \overline{k}_2 = \frac{1}{(h_2 - h_1)}\int_{h_1}^{h_2} k_2 dz \tag{2.29}$$

$$\overline{k}_{r,nw2} = \frac{1}{\overline{k}_2}\frac{1}{(h_2 - h_1)}\int_{h_1}^{h_2} k_2 k_{r,nw} dz \tag{2.30}$$

$$\overline{k}_{r,w2} = \frac{1}{\overline{k}_2}\frac{1}{(h_2 - h_1)}\int_{h_1}^{h_2} k_2 k_{r,w} dz \tag{2.31}$$

Hence, the total vertically averaged parameters are given by

$$\overline{\phi} = \frac{1}{h_2}[\overline{\phi}_1 h_1 + \overline{\phi}_2 (h_2 - h_1)]; \quad \overline{k} = \frac{1}{h_2}[\overline{k}_1 h_1 + \overline{k}_2 (h_2 - h_1)] \tag{2.32}$$

$$\overline{k}_{r,nw} = \frac{1}{h_2}[\overline{k}_{r,nw1} h_1 + \overline{k}_{r,nw2} (h_2 - h_1)] \tag{2.33}$$

$$\overline{k}_{r,w} = \frac{1}{h_2}[\overline{k}_{r,w1} h_1 + \overline{k}_{r,w2} (h_2 - h_1)] \tag{2.34}$$

Generalizing the previous expressions for aquifer with N permeability layers (Figure 2.4 B), the total vertically averaged porosity, permeability and relative permeability are given by

$$\overline{\phi} = \frac{1}{h_N}[\sum_{j=1}^{N} \overline{\phi}_j (h_j - h_{j-1})]; \quad \overline{k} = \frac{1}{h_N}[\sum_{j=1}^{N} \overline{k}_j (h_j - h_{j-1})] \tag{2.35}$$

$$\overline{k}_{r,nw} = \frac{1}{h_N}[\sum_{j=1}^{N} \overline{k}_{r,nwj} (h_j - h_{j-1})] \tag{2.36}$$

$$\overline{k}_{r,w} = \frac{1}{h_N}[\sum_{j=1}^{N} \overline{k}_{r,wj} (h_j - h_{j-1})] \tag{2.37}$$

respectively, where $h_0 = 0$.

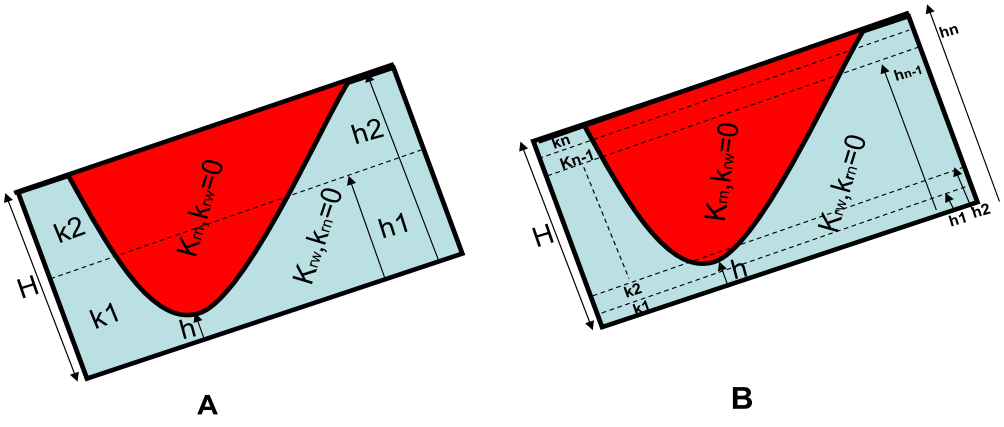

Figure 2.4: Aquifer with layered permeability for two layers (A) and N layers (B).

2.4.4 Fractional flow function for one dimensional system

In this section we will derive the fractional flow function, because the saturation profile can be calculated from it.

First, for the non-layered aquifer, starting with mass conservation equations

$$\phi\frac{\partial S_w}{\partial t}+\frac{\partial u_w}{\partial x}=0 \tag{2.38}$$

$$\phi\frac{\partial S_{nw}}{\partial t}+\frac{\partial u_{nw}}{\partial x}=0 \tag{2.39}$$

adding equations (2.38) and (2.39) together and substituting $S_w + S_{nw} = 1$, we get

$$u_w + u_{nw} = u_{total} \tag{2.40}$$

where u_{total} is called total (Darcy) velocity.

Darcy's equations are given by

$$u_w = -\lambda_w k(\frac{\partial p_w}{\partial x} + \rho_w g \sin(\theta)) \tag{2.41}$$

$$u_{nw} = -\lambda_{nw} k(\frac{\partial p_{nw}}{\partial x} + \rho_{nw} g \sin(\theta)) \tag{2.42}$$

Assuming that $p_w = p_{nw}$ and eliminating the pressure by multiplying Darcy's equations (2.41) with λ_{nw} and (2.42) with λ_w, and subtracting the resulting two equations, we get

$$\lambda_w u_{nw} - \lambda_{nw} u_w = -\lambda_{nw}\lambda_w k\rho_{nw}\sin(\theta) + \lambda_{nw}\lambda_w k\rho_w \sin(\theta). \tag{2.43}$$

Substituting equation (2.40) in (2.43) for u_{nw} and rearranging we get the non-wetting fluid fractional flow

$$F_{nw}(S_w) = \frac{u_{nw}}{u_{total}} = \frac{\lambda_{nw}}{\lambda_{nw}+\lambda_w} + \frac{\lambda_{nw}\lambda_w}{\lambda_{nw}+\lambda_w}\frac{k}{u_{total}}\Delta\rho\sin(\theta) \tag{2.44}$$

where

$f_{nw_{adv}}(S_w) = \frac{\lambda_{nw}}{\lambda_{nw}+\lambda_w}$ is the advection part of the fractional flow, and

$f_{nw_g}(S_w) = \frac{\lambda_{nw}\lambda_w}{\lambda_{nw}+\lambda_w}$ is the gravity part of the fractional flow.

Note that the vertically averaged advection and gravity part of the fractional flow assuming non-layered aquifer is in the same form as (2.44) with $\lambda_w$and λ_{nw} replaced by $\overline{\lambda}_w$and $\overline{\lambda}_{nw}$ respectively.

Next, two plume tail positions must be considered assuming an aquifer with two permeability layers, as shown in Figure 2.5

- $h \geq h_1$

$$\overline{k}_{r,nw} = (h_2 - h)\, k_2 k_{r,nw} \quad \overline{\lambda}_{nw} = \lambda_{nw}\,(h_2 - h)\, k_2 \tag{2.45}$$

$$\overline{k}_{r,w} = [h_1 k_1 + (h - h_1)\, k_2] k_{r,w} \quad \overline{\lambda}_w = \lambda_w [h_1 k_1 + (h - h_1)\, k_2] \tag{2.46}$$

thus, the advection and gravity parts of the fractional flow are

$$f_{nw_{adv}} = \frac{(h_2 - h)\, k_2}{M\,(h_2 - h)\, k_2 + [h_1 k_1 + (h - h_1)\, k_2]} \tag{2.47}$$

$$f_{nw_g} = \frac{(h_2 - h)\, k_2 [h_1 k_1 + (h - h_1)\, k_2]}{\{M\,(h_2 - h)\, k_2 + [h_1 k_1 + (h - h_1)\, k_2]\}\{h_1 k_1 + (h_2 - h_1) k_2\}} \tag{2.48}$$

- $h \leq h_1$

$$\overline{k}_{r,nw} = [(h_1 - h)\, k_1 + (h_2 - h_1)\, k_2] k_{r,nw} \quad \overline{k}_{r,w} = h k_1 k_{r,w} \tag{2.49}$$

$$\overline{\lambda}_{nw} = \lambda_{nw} [(h_1 - h)\, k_1 + (h_2 - h_1)\, k_2] \quad \overline{\lambda}_w = \lambda_w h k_1 \tag{2.50}$$

thus, the advection and gravity parts of the fractional flow are

$$f_{nw_{adv}} = \frac{(h_1 - h)\, k_1 + (h_2 - h_1)\, k_2}{M[(h_1 - h)\, k_1 + (h_2 - h_1) k_2] + h k_1} \tag{2.51}$$

$$f_{nw_g} = \frac{[(h_1 - h)\, k_1 + (h_2 - h_1)\, k_2]\,(h k_1)}{\{M[(h_1 - h)\, k_1 + (h_2 - h_1)\, k_2] + h k_1\}\{h_1 k_1 + (h_2 - h_1) k_2\}} \tag{2.52}$$

respectively.

Finally, we generalize the previous expressions for an aquifer that has N permeability layers, then N cases should be considered according to different tail positions of the plume in different layers. For the tail of the plume located in layer i, then

$$\overline{k} = \frac{1}{h_N}[\sum_{j=1}^{N}(h_j - h_{j-1})k_j] \tag{2.53}$$

$$\overline{k}_{r,nw} = [(h_i - h)\, k_i + \sum_{j=i+1}^{N}(h_j - h_{j-1})k_j]k_{r,nw} \qquad \overline{\lambda}_{nw} = \frac{\overline{k}_{r,nw}}{\mu_{nw}} \tag{2.54}$$

$$\overline{k}_{r,w} = [(h - h_{i-1})\, k_i + \sum_{j=1}^{i-1}(h_{i-j} - h_{i-j-1})k_{i-j}]k_{r,w} \qquad \overline{\lambda}_{w} = \frac{\overline{k}_{r,w}}{\mu_{w}} \tag{2.55}$$

where $h_0 = 0$.

The advection and gravity parts of the fractional flow functions are given by the following expressions

$$f_{nw_{adv}} = \frac{\frac{\overline{\lambda}_{nw}}{\lambda_{nw}}}{M[\frac{\overline{\lambda}_{nw}}{\lambda_{nw}}] + [\frac{\overline{\lambda}_{w}}{\lambda_{w}}]} \tag{2.56}$$

$$f_{nw_g} = \frac{[\frac{\overline{\lambda}_{nw}}{\lambda_{nw}}][\frac{\overline{\lambda}_{w}}{\lambda_{w}}]}{\{M[\frac{\overline{\lambda}_{nw}}{\lambda_{nw}}] + [\frac{\overline{\lambda}_{w}}{\lambda_{w}}]\}\{\overline{k}h_N\}} \tag{2.57}$$

respectively.

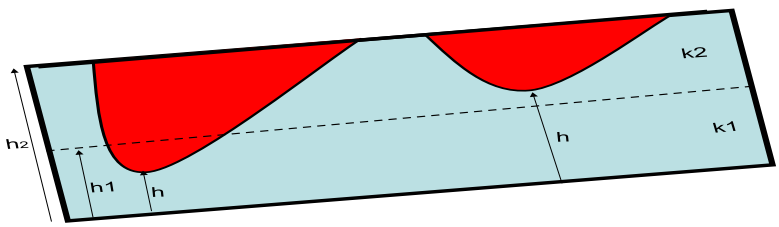

Figure 2.5: Two different positions of the plume tail in two layers aquifer.

Chapter 3

Numerical methods

This chapter introduces the numerical methods that our model is based on. First, we introduce the Riemann problem and the general solution. Then, we present Godunov's method, first order upwind, which uses the solution of the Riemann problem.

Equation (2.24) has the form of a scalar conservation law with flux function

$$F(h) = \frac{(h-H)\left[h+\delta\lambda_w\left(h_{min}-h\right)\right]}{(1-M)\,h+MH+\delta\lambda_w\left(h_{min}-h\right)} sin\left(\theta\right).$$

We are interested in general properties of such conservation laws and how these can aid in solving equation (2.24) numerically.

In the rest of the thesis $u \equiv h \equiv S$.

3.1 Conservation laws

Conservation laws have the following form in one-dimension:

$$\frac{\partial}{\partial t}u + \frac{\partial}{\partial x}f(u) = 0. \tag{3.1}$$

where u represents quantities, or state variables, such as mass, momentum, and energy in a fluid dynamics problem.

The main assumption in equation (3.1) is that knowing the value of $u(x,t)$ at a given point and time allows us to determine the rate of flow, or flux, of each state variable at (x,t), see [16].

3.2 Definition of the Riemann problem

The Riemann problem is simply the conservation law together with particular initial data consisting of two constant states separated by a single discontinuity [16]

$$u(x, t = 0) = u_0(x) = \begin{cases} u_l & x < 0 \\ u_r & x > 0 \end{cases}$$

In this initial data we have two cases, $u_l > u_r$ or $u_l < u_r$, and the solution of this problem depends on these two cases.

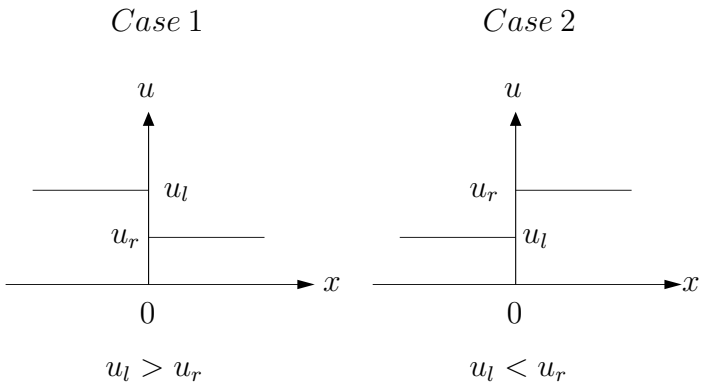

Figure 3.1: Initial conditions for Riemann problem.

3.3 Solution of Riemann problem

The general solution to the Riemann problem is constructed from i) shock waves ii) rarefaction waves iii) contact discontinuities.

Using the method of characteristics, the conservation law in equation (3.1) can be written as [16]

$$\frac{\partial}{\partial t}u + f^{'}(u)\frac{\partial}{\partial x}u = 0 \tag{3.2}$$

substituting

$$\frac{du}{dt} = \frac{\partial u}{\partial t} + \frac{\partial u}{\partial x}\frac{dx}{dt}$$

in equation (3.2), we get

$$\frac{du}{dt} = \frac{\partial u}{\partial x}\left(\frac{dx}{dt} - f^{'}(u)\right)$$

$\Longrightarrow$

$$\frac{du}{dt} = 0$$

for

$$\frac{dx}{dt} = f^{'}(u)$$

$\Longrightarrow u$ is constant along the characteristics.

Integrating the above equation, we get the characteristics equation:

$$x = x_o + f^{'}(u)t \tag{3.3}$$

which means that the characteristics are straight lines for a given constant saturation value.

The function u is called a weak solution of the conservation law if

$$\int_0^{\infty}\int_{-\infty}^{+\infty}[\varphi_t u + \varphi_x f(u)]dxdt = -\int_{-\infty}^{+\infty}\varphi(x,0)u(x,0)dx \tag{3.4}$$

holds for all functions $\varphi \epsilon C_0^1(\mathbb{R}\times\mathbb{R}^+)$, where φ is a test function and C_0^1 is the space of function that are continuously differentiable with "compact support" [16]. An equivalent integral formulation of the weak solution is given by

$$\int_{x_0}^{x_1} u(x,t)dx - \int_{x_0}^{x_1} u(x,0)dx = \int_0^t f(u(x_0,t))dx - \int_0^t f(u(x_1,t))dx \tag{3.5}$$

The characteristics equation plays an important role in finding the solution of the Riemann problem. The solution procedure involves by drawing the characteristics from the initial conditions, thus if we have

1. parallel characteristic equations, then contact discontinuities.

2. intersecting characteristic equations, then the unique weak solution is a shock wave. See Figure 3.2.

3. diverging characteristic equations, then infinitely many weak solutions. One of them is a shock wave, which is not stable to perturbations. Other weak solution is a rarefaction wave (continuous solution), which is stable to perturbations . See Figure 3.3.

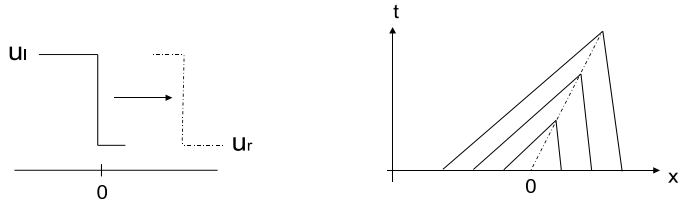

Figure 3.2: Shock wave.

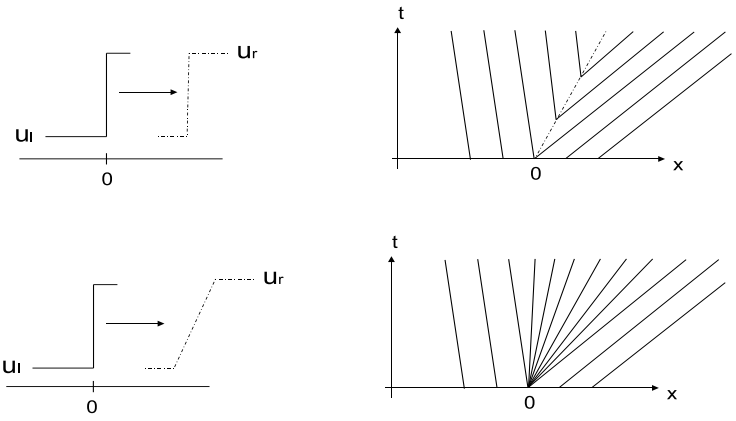

Figure 3.3: First row, shock wave. Second row, rarefaction wave.

Once the shock wave forms, it propagates at a certain speed. Consider a shock wave located at the point x_0 at time t_1. The integral form of the conservation law imples that

$$\int_{x_0}^{x_0+\Delta x} u(x,t_1+\Delta t)dx - \int_{x_0}^{x_0+\Delta x} u(x,t_1)dx = \int_{t_1}^{t_1+\Delta t} f[u(x_0,t)]dt - \int_{t_1}^{t_1+\Delta t} f[u(x_0+\Delta x,t)]dt. \tag{3.6}$$

If follows that

$$V_s = \frac{f(u_l) - f(u_r)}{u_l - u_r}$$

where u_r and u_l are the states immediately to the right and left of the shock respectively. This is called **Rankine-Hugoniot jump condition**.

In situation 3 above, the weak solution is not unique, then the **Entropy condition [16]**

$$\frac{f(u) - f(u_r)}{u - u_r} \leq V_s \leq \frac{f(u) - f(u_r)}{u - u_r}$$

where $u \in (u_l,u_r)$, is required to choose the physically relevant vanishing viscosity solution.

If a general flux function which has the same form as the fractional flow function in equation (2.44) is given by

$$f_{i,j} = \frac{\lambda_i(u_i)}{\lambda_i(u_i) + \lambda_j(u_j)} V_{i,j} + \frac{\lambda_i(u_i)\lambda_j(u_j)}{\lambda_i(u_i) + \lambda_j(u_j)} \Delta\rho g \tag{3.7}$$

where

u_j, u_i: are the saturation's of phases j and i respectively, and $u_j = 1 - u_i$

$\lambda_{i,j}$: is the mobility of the phase i,j

$\Delta\rho$: density difference

g: gravity

$V_{i,j}$: velocity of the phase i,j respectively

then, we should consider the gravity (second part in equation (3.7)) effect on the solution.

In addition to the initial conditions, we consider the general flux function without the gravity term (monotone fractional flow function) and with the gravity term (general fractional flow function) in the following two subsections respectively.

3.3.1 Monotone fractional flow function

Monotone fractional flow function is the first term of equation (3.7).

- Case 1 ($u_l > u_r$):

In this case, the characteristic equations intersect and the solution is a shock wave, which is defined by

$$u = \begin{cases} u_l & \texttt{for} \quad \frac{x}{t} < V_s \\ u_r & \texttt{for} \quad \frac{x}{t} > V_s \end{cases}$$

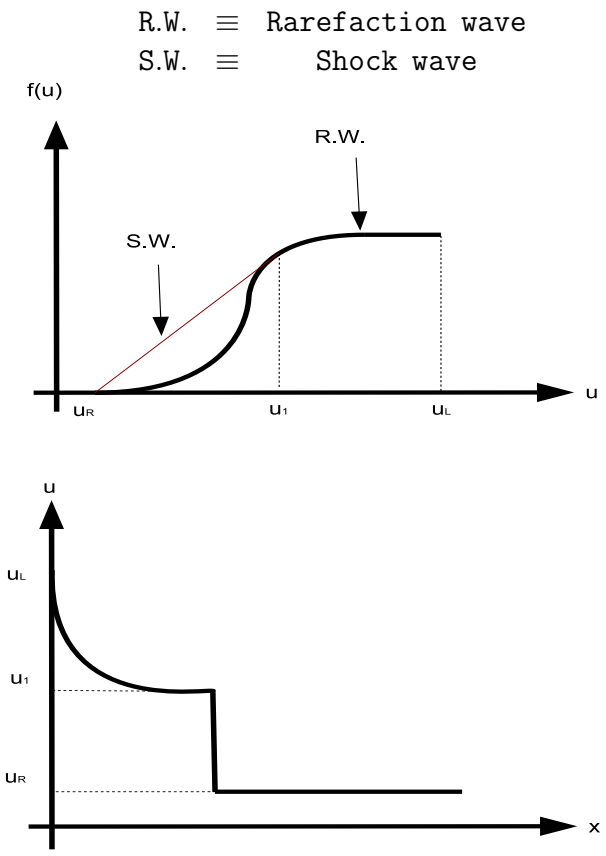

Figure 3.4: Monotone fractional flow function (top) and the solution (bottom) when $u_l > u_r$.

- Case 2 ($u_l < u_r$):

In this case, the characteristic equations diverge and the solution is a rarefaction wave, which is defined by

$$u = \begin{cases} u_l & \texttt{for} \quad \frac{x}{t} < f^{'}(u_l) \\ G(\frac{x}{t}) & \texttt{for} \quad f^{'}(u_l) < \frac{x}{t} < f^{'}(u_r) \\ u_r & \texttt{for} \quad \frac{x}{t} > f^{'}(u_r) \end{cases}$$

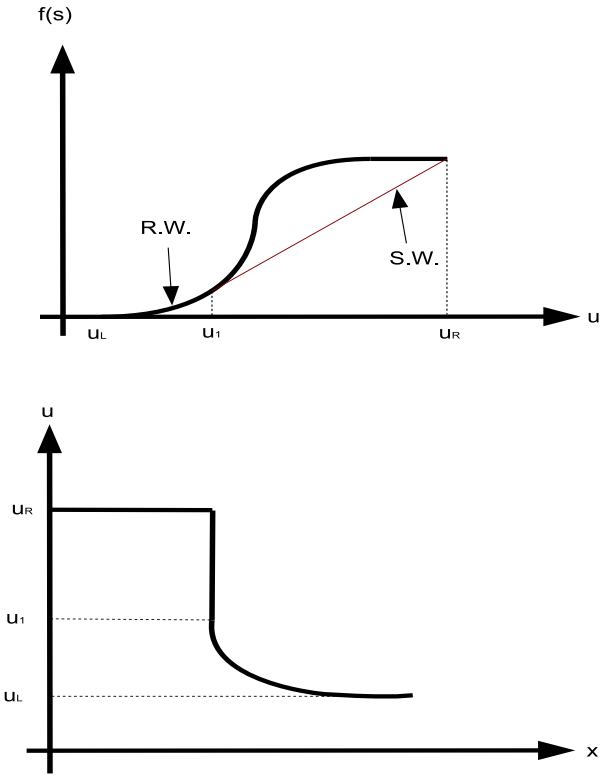

Figure 3.5: Monotone fractional flow function (top) and the solution (bottom) when $u_l < u_r$.

3.3.2 Fractional flow function

- Case 1 ($u_l > u_r$):

Figure 3.6 shows an upper convex envelope.

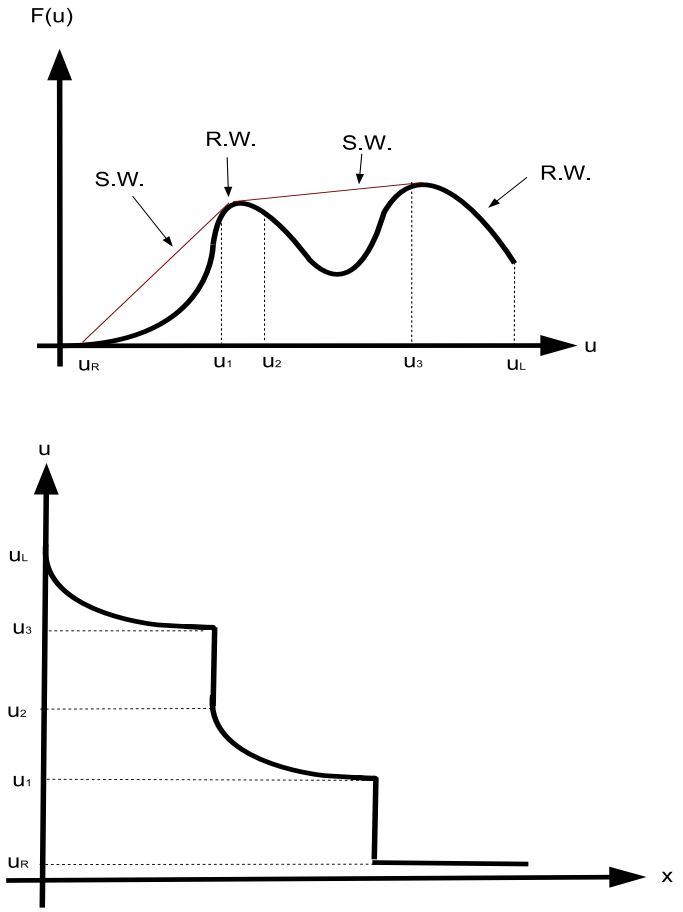

Figure 3.6: General flux function with gravity (top) and the general solution (bottom) in equation (3.7) for $u_l > u_r$.

- Case 2 ($u_l < u_r$):

Figure 3.7 shows a lower convex envelope.

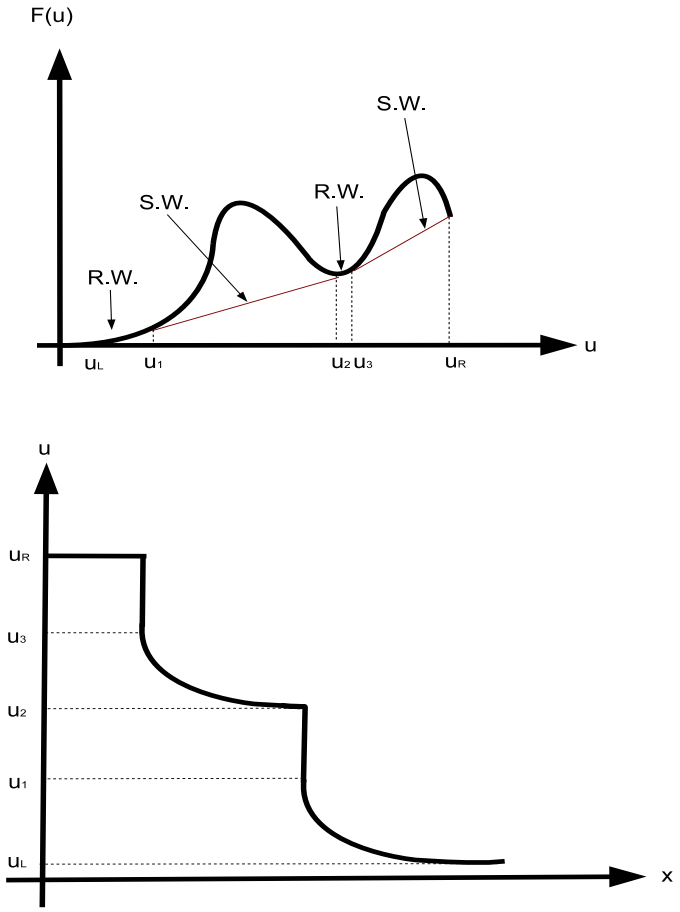

Figure 3.7: General flux function with gravity (top) and the general solution (bottom) in equation (3.7) for $u_l < u_r$.

3.4 Godunov's method

Godunov's method uses the solution of the Riemann problem defined at cell interfaces with piecewise constant initial data to compute the time averaged flux function. The hyperbolic part of equation (4.1) is equivalent to a Cauchy problem. Different approaches have been made to solve the time dependent Cauchy problem in one spatial dimension,

$$u_t + f(u)_x = 0 \tag{3.8}$$

$$u(x,0) = u_0(x) \tag{3.9}$$

In 1959, Godunov proposed a way to follow the characteristics forward in time, instead of backwards. This means solving several Riemann problems forward in time. The earlier attempts to use upwind differencing, 1^{st} and 2^{nd} order, gave unacceptably diffused shock profiles or oscillatory solutions. Godunov's method reduces this error, by using more information about the local behavior of the solution. Godunov's method is described in more detail in [16].

Assuming a uniform grid, $x_j = \left(j + \frac{1}{2}\right)\Delta x$, $j = 1, 2, ..., N$ with mesh spacing Δx, and define the cell average

$$U_j^n = \frac{1}{\Delta x}\int_{x_{j-\frac{1}{2}}}^{x_{j+\frac{1}{2}}} u^n(x,t_n)\,dx. \tag{3.10}$$

Integrating (3.8) over the grid cell $[x_{j-\frac{1}{2}}, x_{j+\frac{1}{2}}) \times [t_n, t_{n+1}]$ results in

$$U_j^{n+1} = U_j^n - \frac{\Delta t}{\Delta x}\left[F_{j+\frac{1}{2}}^n - F_{j-\frac{1}{2}}^n\right], \tag{3.11}$$

where

$$F_{j\pm\frac{1}{2}}^n = \frac{1}{\Delta t}\int_{t_n}^{t_{n+1}} f\left(u\left(x_{j\pm\frac{1}{2}}, t\right)\right)dt \tag{3.12}$$

and $\Delta t = t_{n+1} = t_n$.

By assuming a piecewise constant approximation for u at $t = t_n$, i.e.

$$u(x,t_n) \approx \begin{cases} \vdots & \\ U_{j-1}^n & \texttt{if} \quad x \quad \in \quad [x_{j-\frac{3}{2}},\, x_{j-\frac{1}{2}}) \\ U_j^n & \texttt{if} \quad x \quad \in \quad [x_{j-\frac{1}{2}},\, x_{j+\frac{1}{2}}) \\ U_{j+1}^n & \texttt{if} \quad x \quad \in \quad [x_{j+\frac{1}{2}},\, x_{j+\frac{3}{2}}) \\ \vdots & \end{cases}$$

we can calculate the fluxes $F_{j\pm\frac{1}{2}}^n$ in (3.12) using the solution of the Riemann problem with initial states given by U_j^n and the corresponding values in the

neighboring cells, i.e., let $u^*(u_l,\, u_r)$ be the (constant) solution of the Riemann problem in (3.8) along the line $x = 0$ for $t > 0$, and set

$$F^n_{j-\frac{1}{2}} = \frac{1}{\Delta t}\int_{t_n}^{t_{n+1}} f\left(u^*\left(U^n_{j-1}, U^n_j\right)\right) dt = f\left(u^*\left(U^n_{j-1}, U^n_j\right)\right)$$

and

$$F^n_{j+\frac{1}{2}} = \frac{1}{\Delta t}\int_{t_n}^{t_{n+1}} f\left(u^*\left(U^n_{j}, U^n_{j+1}\right)\right) dt = f\left(u^*\left(U^n_{j}, U^n_{j+1}\right)\right).$$

It is important that the time interval is short, to avoid waves from neighboring Riemann problems interacting during the time step. This is ensured if the CFL-condition $|\, \frac{\Delta t}{\Delta x}\mathtt{max}\left\{F'\left(U^n_j\right)\right\}\, | \leq 1$ is satisfied.

So, Godunov's method for the problem

$$u_t + f(u)_x = 0$$

leads to the following discritization

$$U^{n+1}_j = U^n_j - \frac{\Delta t}{\Delta x}\left[f\left(u^*\left(U^n_j, U^n_{j+1}\right)\right) - f\left(u^*\left(U^n_{j-1}, U^n_j\right)\right)\right] \tag{3.13}$$

The disadvantage of Godunov's 1^{st} order method is that it requires a very fine mesh.

3.4.1 The sonic point glitch

Given the scalar equation

$$u_t + f(u)_x = 0 \tag{3.14}$$

and initial data $u(x,0) = u_0(x)$, where $u_0(x)$ is a given function, $x\,\epsilon\,\mathbb{R}$ and $t > 0$.

$$u_0(x) = \begin{cases} u_l & x < 0 \\ u_r & x > 0 \end{cases} \tag{3.15}$$

where u_l and u_r are two constants. Writing the solution of the Riemann problem from section (3.3.1) case 1 and 2 respectively, it is

(i) a shock wave solution

$$u(x,t) = \begin{cases} u_l & \texttt{for} \quad \frac{x}{t} < V_s \\ u_r & \texttt{for} \quad \frac{x}{t} > V_s \end{cases} \tag{3.16}$$

(ii) a rarefaction wave solution

$$u(x,t) = \begin{cases} u_l & \texttt{for} \quad \frac{x}{t} < u_l \\ \frac{x}{t} & \texttt{for} \quad u_l \leq \frac{x}{t} \leq u_r \\ u_r & \texttt{for} \quad \frac{x}{t} > u_r \end{cases} \tag{3.17}$$

The sonic point corresponds to a point $f'(u) \equiv \frac{1-2u-u^2(M-1)}{[u(M-1)+1]^2} = 0 \Rightarrow u_{1,2} = \mp\frac{1}{1+\sqrt{M}}$, and the location of this point is fixed in space due to its diminishing wave speed. For simplicity, we take $M = 1$, then $f'(u) \equiv 1-2u = 0 \Rightarrow u = \frac{1}{2}$. Let u be represented by u_m as the sonic point. Thus, for the Riemann problem (3.14) and (3.15), if $u_l < u_m = \frac{1}{2} < u_r$ or $u_l > u_m = \frac{1}{2} > u_r$ as shown in Figure 3.8(b & e), the solution given in (3.16) or (3.17) corresponds to a transonic solution. Transonic solution means that a jump appears at the sonic point $x = \frac{1}{2}$ after one evolution time step. In correcting the sonic point glitch, in the (i) shock wave we take the minimum value $f(u) = \texttt{min}\left[f(u_l), f(u_r)\right]$ while in the (ii) rarefaction wave we take the maximum value $f(u) = \texttt{max}\left[f(u_l), f(u_r), f(u_m)\right]$ as shown in Figure 3.8.

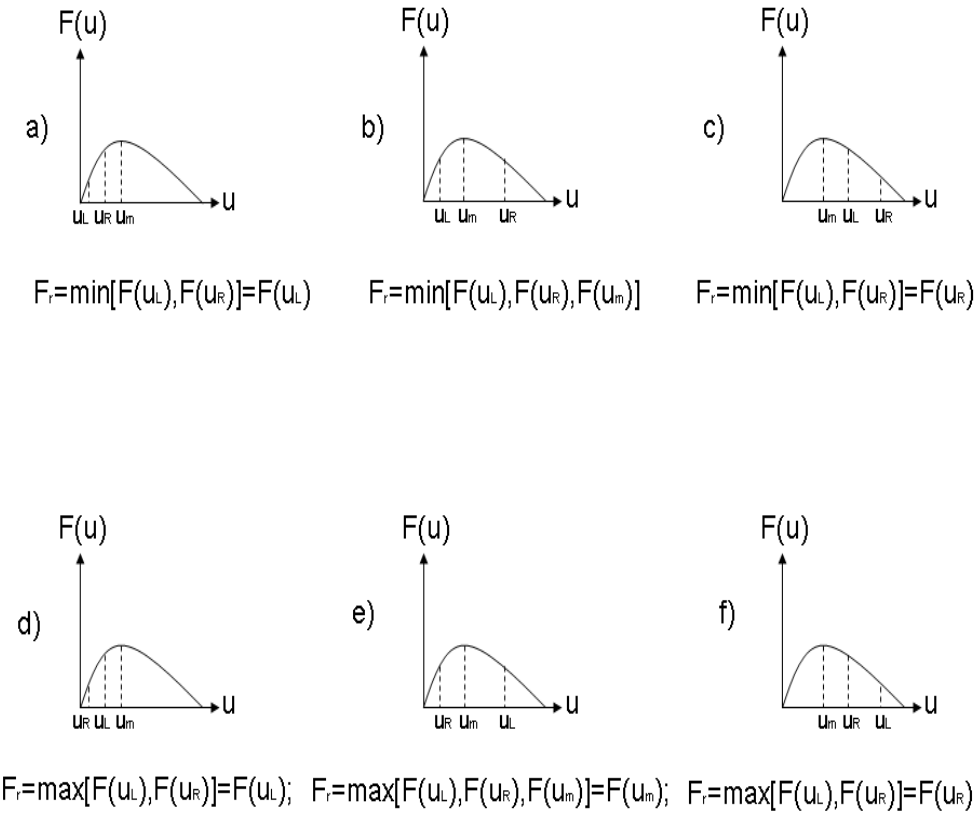

Figure 3.8: Different locations of u_r and u_l around the sonic point. (a-c) shock wave; (d-f) rarefaction wave.

Chapter 4

Numerical simulations

This chapter presents the results of full two-dimensional and vertically averaged numerical simulations. We start this section with a brief description of the two numerical simulators, Eclipse and a VE simulator implemented in MATLAB to solve the reduced equation (2.24) as obtained by assuming vertical equilibrium.

4.1 Eclipse simulator

Eclipse is an oil and gas reservoir simulator that includes options for simulating many different scenarios, through several thousand keywords. The fundamental challenge in reservoir simulation is to create a model that predicts the state of a reservoir through time, taking into account all changes produced [29].

The Eclipse simulator consists of two separate simulators [8],

- ECLIPSE 100 is fully implicit, three phase, three dimensional, specializing in black oil modeling with gas condensate options.
- ECLIPSE 300 is fully implicit, implicit pressure explicit saturation (IMPES) and adaptive implicit (AIM) modes, specializing in compositional modeling with cubic equation of state, pressure dependent K-value and black oil fluid treatments.

The fundamental difference between these models is that Eclipse 100 solves the black oil equations (a fluid model), while Eclipse 300 solves the reservoir flow equations for compositional hydrocarbon descriptions and thermal simulation.

4.1.1 Grid description

The numerical solution for the two-dimensional simulations are computed in a numerical grid that has 50,000 cells distributed as follows:

1. 500 cells in the x-direction, 1 cell in the y-direction and 100 cells in the z-direction.
2. 400 m length for each cell in the x-direction, 10 m in the y-direction and 2 m in the z-direction.

4.2 VE simulator

The vertically equilibrium (VE) solution corresponds to the numerical solution of the following equation

$$\frac{\partial \eta}{\partial \tau} + \sigma \frac{\partial}{\partial \xi}\{f(\eta) - (\frac{1}{Pe})\left(D(\eta)\frac{\partial \eta}{\partial \xi}\right)\} = 0, \tag{4.1}$$

where

$$\eta = \frac{h}{H}; \quad \xi = \frac{x}{L}; \quad \tau = \frac{t}{L(\kappa_1 sin(\theta))^{-1}}$$

$$f(\eta) = \frac{\eta(1-\eta)}{\eta(M-1)+1} \tag{4.2}$$

$$\sigma = \begin{cases} 1, & \frac{\partial \eta}{\partial \tau} < 0 \\ 1-\epsilon, & \frac{\partial \eta}{\partial \tau} > 0 \end{cases} \quad \texttt{discontinuous coefficient}$$

$$\epsilon = \frac{S_{nwr}}{1 - S_{wr}} \qquad \texttt{residual} \quad 0 \leq \epsilon < 1$$

$$Pe = \left(\frac{L}{H}\right) tan(\theta) \geq 0 \qquad \texttt{Peclet number}$$

$$M = \frac{k_{r,nw}\mu_w}{\mu_{nw}k_{r,w}} \geq 0 \qquad \texttt{mobility ratio}$$

Equation (4.1) is the dimensionless form of equation (2.24) [10] and consists of two main terms, the convection term $f(\eta)_\xi$, and the diffusion term $(D(\eta)\eta_\xi)_\xi$. Both terms cause transport of the non-wetting mass from one point to another. The difference between these two terms is that the convective term translates the center of mass of the plume, while the diffusive one smoothes it out. One way to solve the system is to use an operator splitting technique. The time evolution is split into two partial steps in order to separate the effects of convection and diffusion. Compared to a method that solves the whole system in one step this operator splitting technique takes the physics of the equations into account. Then a suitable method can be chosen for each term independent of each other [27].

Equation (4.1) can be written as

$$\frac{\partial \eta}{\partial \tau} + \frac{\partial}{\partial \xi}\left(F(\eta)\right) = 0 \tag{4.3}$$

where $F(\eta) = (\sigma f(\eta)) - (\frac{\sigma}{Pe})\left(D(\eta)\frac{\partial \eta}{\partial \xi}\right)$ is the total flux function. Integrating (4.3) over the interval $(x,t)\,\epsilon\,[x_o,\, x_1]\times[t^n,\, t^{n+1}]$

$$\int_{x_0}^{x_1} \eta^{n+1} dx - \int_{x_0}^{x_1} \eta^n dx = \int_{t^n}^{t^{n+1}} F(\eta)\mid_{x=x_0} dt - \int_{t^n}^{t^{n+1}} F(\eta)\mid_{x=x_1} dt \tag{4.4}$$

The mass is conserved over this domain (mass conservation law), thus the mass flowing into the domain at x_0 equals the mass flowing out at x_1, thus $F(\eta) = 0$ which leads to $D(\eta) \equiv f(\eta)$.

The solution from Godunov's method has been used as input for solving the diffusion part, the result coming out from the diffusion part is taken as our final result for the first time step. For the second time step, we use the final result from the first time step as initial condition and we do the same steps as in the first time step, and so on. The flux function in equation (4.2) has been used in the simulation of the homogeneous aquifer (non-layered), while for the two-layered aquifer a different flux function in each layer has been used, as shown here:

$$\begin{array}{ll} \texttt{For} & h \leq h_1 \quad (2.52) \\ \texttt{For} & h \geq h_1 \quad (2.48) \end{array}$$

Figure 4.1 shows that the fractional flow function in the layered aquifer is continuous for all the simulations, where the dashed (B2, C2, D2 and E2)

and solid (B1, C1, D1 and E1) curves represent the fractional flow function in the upper layer and lower layer of the aquifer for the different scenarios (note that A represents the non-layer aquifer). It also shows that the sonic point always exists when the CO_2 plume is in the lower layer of the aquifer.

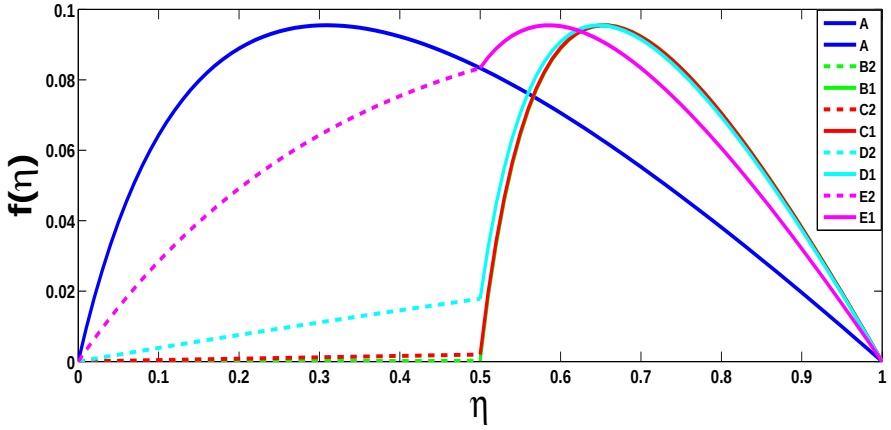

Figure 4.1: Fractional flow function for the different simulations. Dashed and straight lines correspond to the location of the CO_2 plume.

4.3 Problem definition

We model a 2D vertical section along the dip of the aquifer. The aquifer is modeled as a rectangular domain of 200 m thickness and 200 km length, dipping with an angle $\alpha = 1.5^o$ with respect to the horizontal, as shown in Figure 4.2. We consider the upper left-hand corner of the domain to be at a depth of 6000 m and the upper right-hand corner at a depth of 764.6 m from the land surface. Formation properties include a porosity of 15%, compressibility of $4.5 \times 10^{-10}\text{Pa}^{-1}$and a permeability as shown in Table 4.1 where k_1 occupies the lower half layer and k_2 occupies the upper half layer of the aquifer as shown in Figure 4.2.

The CO_2 plume is initially a uniform saturation $S_{nw} = 80\%$, corresponding to an irreducible saturation of $S_{nwr} = 20\%$, in the sub-domain labeled CO_2 in Figure 4.2 (red square). Within the initial CO_2 plume, pressure and saturation values are maintained at their initial values. The rectangular shape of the initial plume is a simplification that can be justified considering the scale of injection and the typical location of injection wells, because we are interested in the CO_2 plume shape after the injection period. We use similar data

and initial conditions as for the Svalbard benchmark, see [12]. Moreover, the same amount of CO_2 placed in both layers with two different permeability values is not reasonable. Plume evolution takes place under the combined action of gravity and pressure forces, with CO_2 buoyancy due to lower density being the primary driving force.

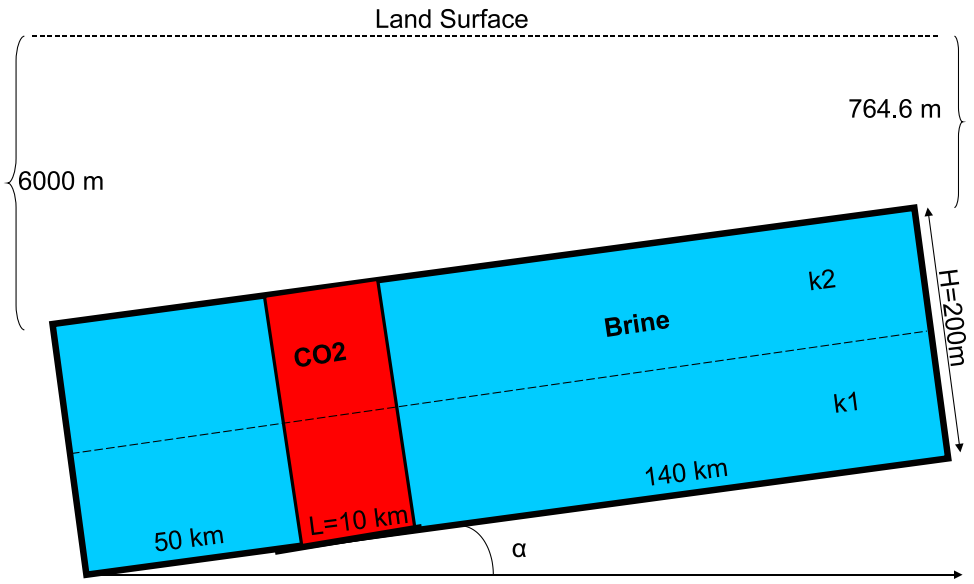

Figure 4.2: Schematic of the simulated two-dimensional section. The domain is dipping by an angle $\alpha = 1.5^o$. The location of the initial CO_2 and brine regions are shown in red and blue, respectively.

Relative permeability for wetting (k_{rw}) and non-wetting (k_{rnw}) were assumed as in [25]

$$k_{r,w} = \sqrt{S^*}\left\{1 - \left(1 - [S^*]^{\frac{1}{m}}\right)^m\right\}^2 \tag{4.5}$$

$$k_{r,nw} = \left(1 - \hat{S}\right)^2\left(1 - \hat{S}^2\right) \tag{4.6}$$

where $S^* = (S_w - S_{r,w})/(1 - S_{r,w})$, $\hat{S} = (S_w - S_{r,w})/(1 - S_{r,w} - S_{r,nw})$, with S_w the wetting saturation, and $S_{r,w}, S_{r,nw}$ the irreducible wetting and

non-wetting saturations, respectively. The values used in the simulations are $(S_{r,w} = S_{r,nw} = 20\%)$, $m = 0.457$.

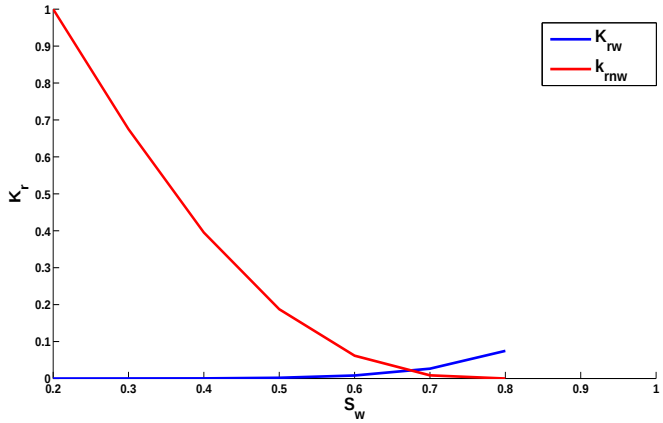

Figure 4.3: Brine (blue) and CO_2 (red) relative permeability curves as a function of brine saturation.

We define five simulation scenarios according to the permeability values as listed in Table 4.1, in order to study the ratio effect between the two permeability layer values.

	Homogeneous aquifer	Two-layer aquifer			
	Simulation A	Simulation B	Simulation C	Simulation D	Simulation E
k_2	250 mD	0.1 mD	1 mD	10 mD	100 mD
k_1	250 mD	500 mD	500 mD	500 mD	500 mD

Table 4.1: Simulated scenarios according to permeability values.

Chapter 5

Comparison of Eclipse & VE results

This chapter presents numerical simulation results of VE and the 2D Eclipse simulations. Taking the vertically averaged of the 2D Eclipse simulation results ends up with 1D results that we can compare with the VE solution.

Figure 5.1 presents the initial conditions for VE and Eclipse simulations. This figure shows that we use the same initial conditions in both cases such that any difference in the results will be due to differences in the mathematical formulation of the problem or/and to different numerical methods used in each simulator.

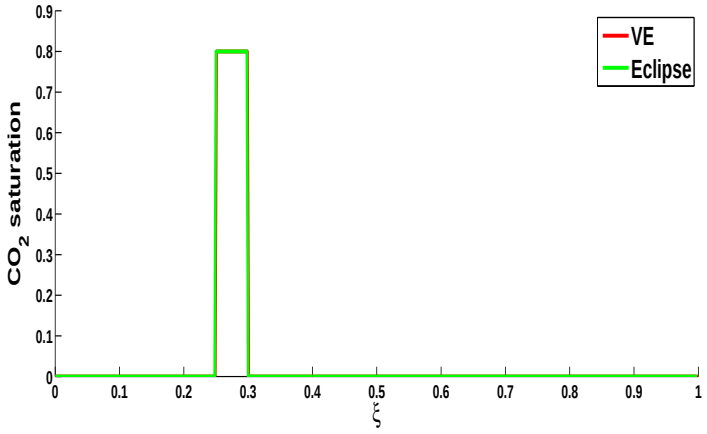

Figure 5.1: VE and Eclipse initial CO_2 saturation's condition.

5.1 Reference case

5.1.1 Simulation A

Figure 5.2 presents the results from Eclipse simulation at different times. During drainage, the CO_2 displaces brine at the tip of the plume in the horizontal direction (from left to right) while during imbibition, the brine replaces CO_2 at the tail of the plume in the horizontal direction (from right to left). Due to density difference between CO_2 and brine, the buoyant CO_2 migrates laterally in the up-dip direction.

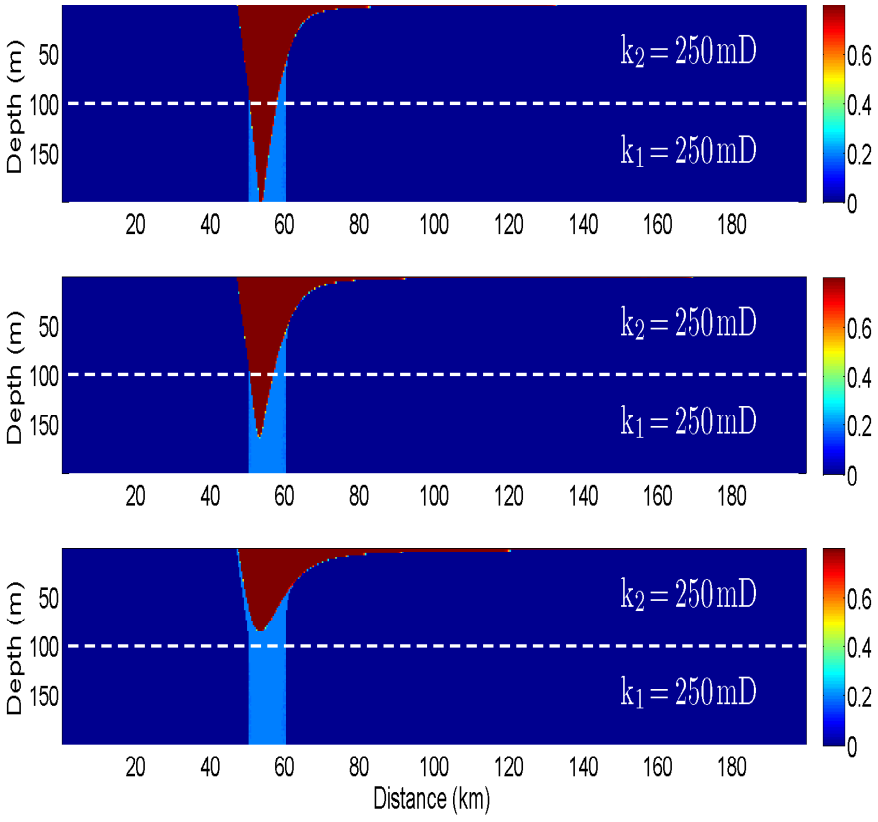

Figure 5.2: Simulation A: simulated CO_2 saturation after 1000 (top), 1500 (middle) and 3000 (bottom) years. Light blue areas indicate immobile CO_2, red areas correspond to mobile CO_2 and dark blue regions indicate pure brine.

The vertically averaged results of both simulators for simulation A are presented in Figure 5.3.

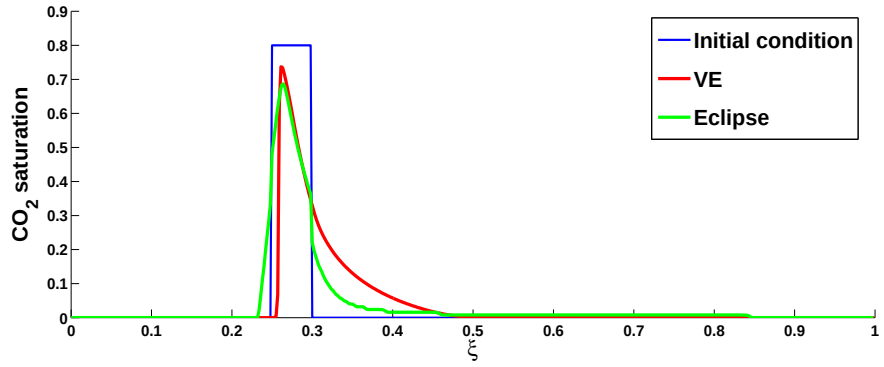

Figure 5.3: Simulation A: vertically averaged saturation values after 1500 years.

From Figure 5.3 we can recognize immediately three different regions:

- A first region (0.23–>0.26) which represents the diffusion part: the vertically averaged result gives unrecognizable diffusion at this early time of simulation where we expect this result because we wrote our code depending on Godunov's method which is first order upwind method. While in the other side we see that the results from Eclipse shows a diffusion in the down-dip direction.
- The second region (0.26–>0.29) which represents the initial condition: both give approximately the same solution with some small numerical calculations error in the beginning and end, while in the middle area the two solutions coincide with each other.
- The third region (0.29–>0.45) which represents the advection part: Eclipse gives a strong decay in the behavior exactly outside the initial condition rectangle, this is because when the CO_2 starts migrating at the top of the aquifer leaving a residual trapped CO_2 behind it in the initial conditions, as shown in Figure 5.2 middle.

We are interested in the advection term more than the diffusion term, so to get more direct comparison between the two solutions shown in Figure 5.3, we plot three vertical profiles of the solutions shown in Figure 5.4.

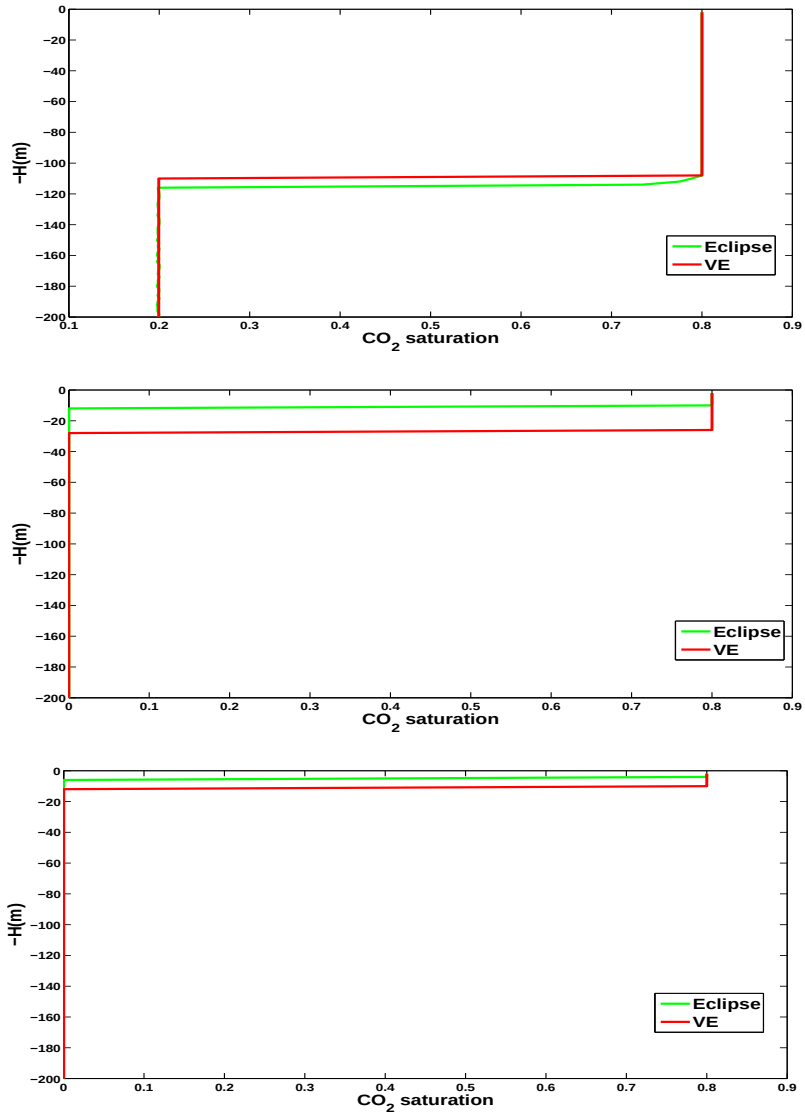

Figure 5.4: Vertical shots with different positions taken at 1500 years of simulation A: inside the initial CO_2 saturation, at 6 km (top), at 20 km (middle) and at 30 km (bottom) away from the second edge of the initial CO_2 saturation.

Recall that according to Figure (5.4 top) the CO_2 saturation values range from 0.2 to 0.8, where the lower bound represents the immobile CO_2 region left behind in the initial rectangle, while in Figure (5.4 middle & bottom) range from 0 to 0.8, where lower bound represents the brine region, as shown in Figure 5.2.

The vertical profiles in Figure (5.4 top & bottom) shows that we have the same solution in both simulators. The distance difference in between the vertical profiles is equal to 6 m, which is triple the grid size of each cell in the vertical direction, while in Figure (5.4 middle) it does not show the same solution with a distance difference of 24 m, which is eight times bigger than the grid size in the vertical direction.

5.1.2 Simulation B

In this case the VE model produces robust result. It gives a totally different CO_2 plume shape from what we got in Eclipse, as shown in Figure 5.6. This means that we are not getting the right answer. The Eclipse simulation in Figure 5.5 shows us how the plume looks, and here it shows that we have two connected plumes. The first plume migrates in the x-direction at the top of the lower layer with the higher permeability, then it starts to migrate upwards entering the upper layer with the lower permeability displacing the brine in the horizontal and vertical directions at the same time. After 1000, 1500 and 3000 years the plume migrates 22, 32 and 60 m respectively in the vertical direction measured from the top of the lower layer. The second plume migrates also in x-direction at the top of the upper layer but with a very low velocity compared to the velocity of the first plume. This is because of the very poor permeability in the upper layer.

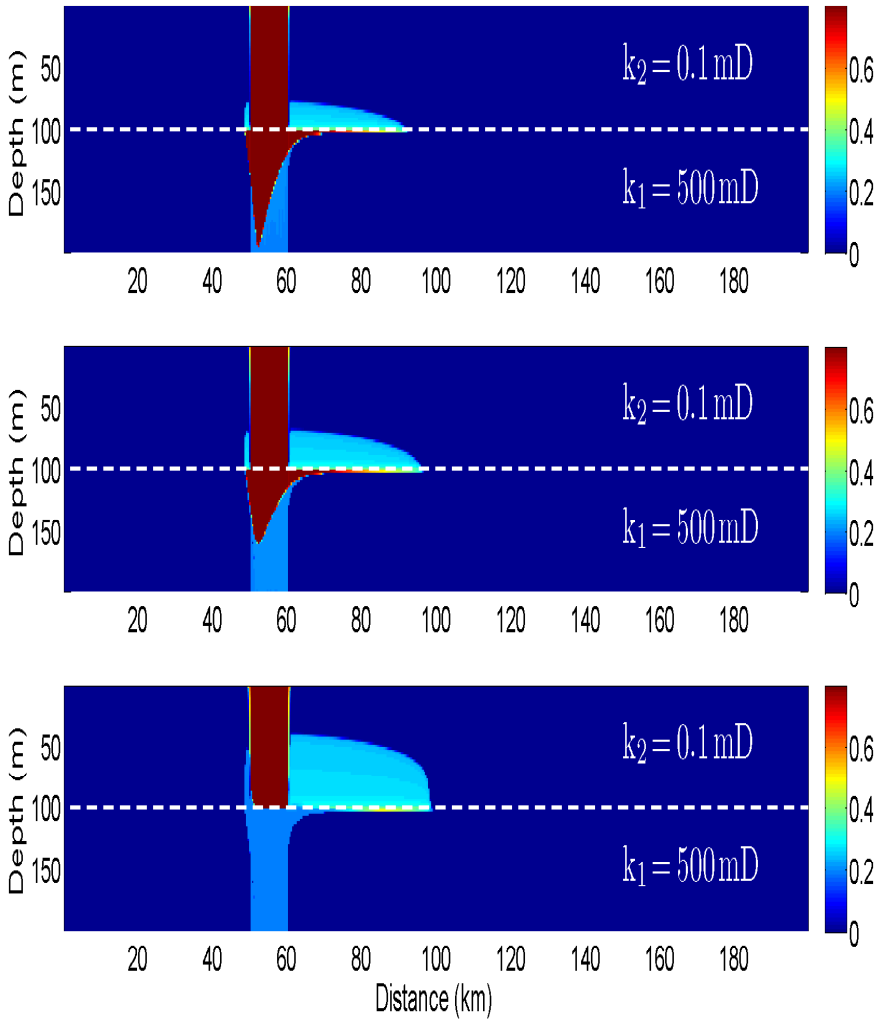

Figure 5.5: Simulation B: simulated CO_2 saturation after 1000 (top), 1500 (middle) and 3000 (bottom) years. Light blue areas indicate immobile CO_2, red areas correspond to mobile CO_2 and dark blue regions indicate pure brine.

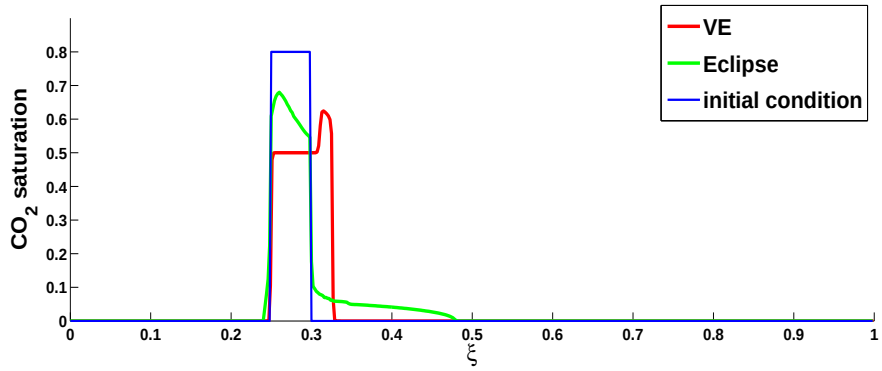

Figure 5.6: Simulation B: vertically averaged saturation values after 1500 years, head of green plume $\simeq$0.68 and red plume $\simeq$0.62.

To investigate more about this result, four vertical profiles have been taken across these two solutions, as shown in Figure 5.7.

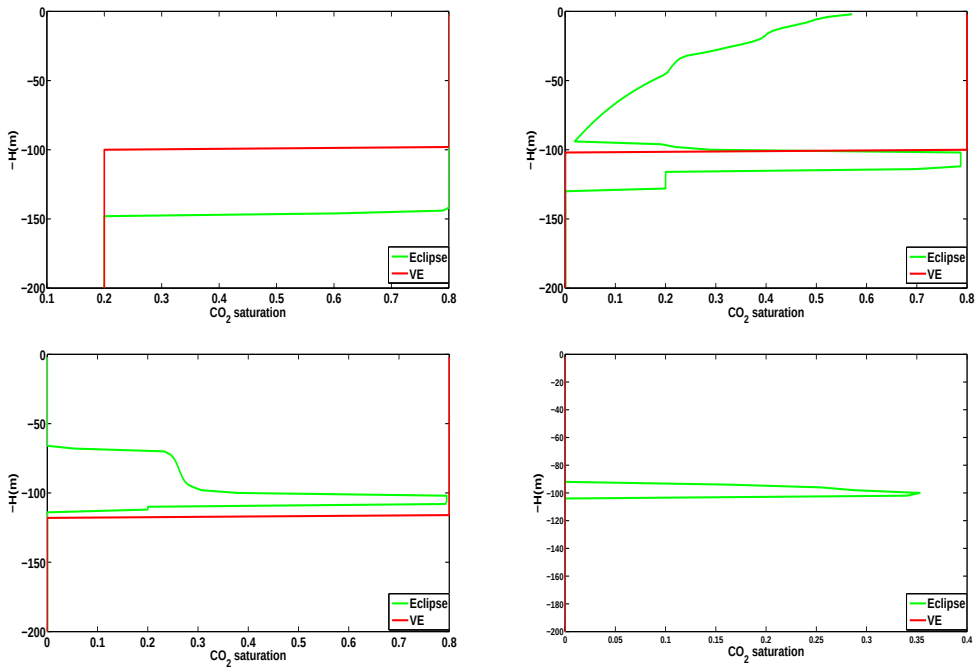

Figure 5.7: Vertical profiles at different x positions after 1500 years for simulation B. First (top left), inside the initial CO_2 saturation, at 4.8 km, second (top left) at 10.4 km, third (bottom left) at 12.4 km and fourth (bottom right) at 44.8 km, away from the first edge of the initial CO_2 saturation.

The results of the vertical profiles shown in Figure 5.7, indicate that the two models produce two different plume shapes. With sharp interface approximation, if we move from the top to the bottom of the aquifer we get the sequence, CO_2– brine in terms of fluid presence, while in Figure (5.7 top-right, bottom-left and bottom-right) we get the following sequence, CO_2– brine – CO_2– brine, brine – CO_2– brine and brine – CO_2– brine respectively. This sequence shows that the sharp interface approximation is not satisfied in this case.

5.1.3 Simulation C

In this case we are still having two plumes as a result but the difference between simulation C and B, is that much more CO_2 migrated upward in the vertical direction reaching (joining the second plume) the top of the upper

layer and less distance migrated at the top of the lower layer. This is because of the higher permeability in simulation C than in simulation B in the upper layer of the aquifer. While in both cases (at 1500 years), the highest CO_2 saturation is observed in the top of the lower layer of the aquifer. We noticed a major different in the distance migrated in simulations B and C given by Eclipse, 36 km and 8 km measured from the second edge of the initial CO_2 saturations respectively. This is because of the more upward migrated CO_2 in simulation C.

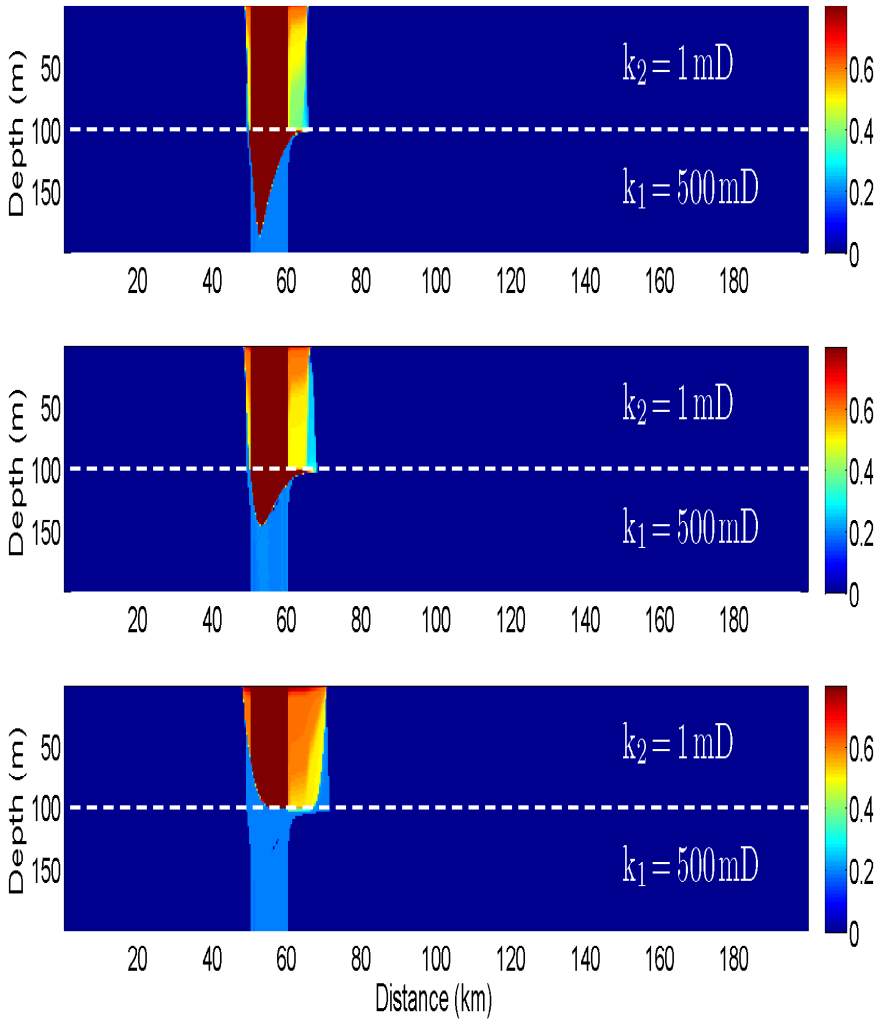

Figure 5.8: Simulation C: simulated CO_2 saturation after 1000 (top), 1500 (middle) and 3000 (bottom) years. Light blue areas indicate immobile CO_2, red areas correspond to mobile CO_2 and dark blue regions indicate pure brine.

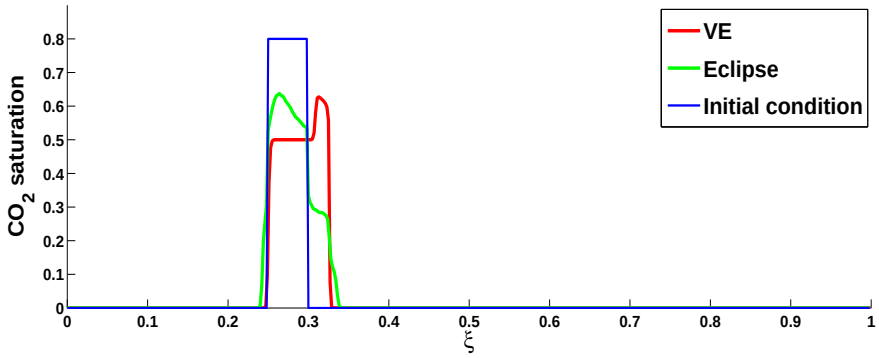

Figure 5.9: Simulation C: vertically averaged saturation values after 1500 years, head of green plume ≃0.637 and red plume ≃0.627.

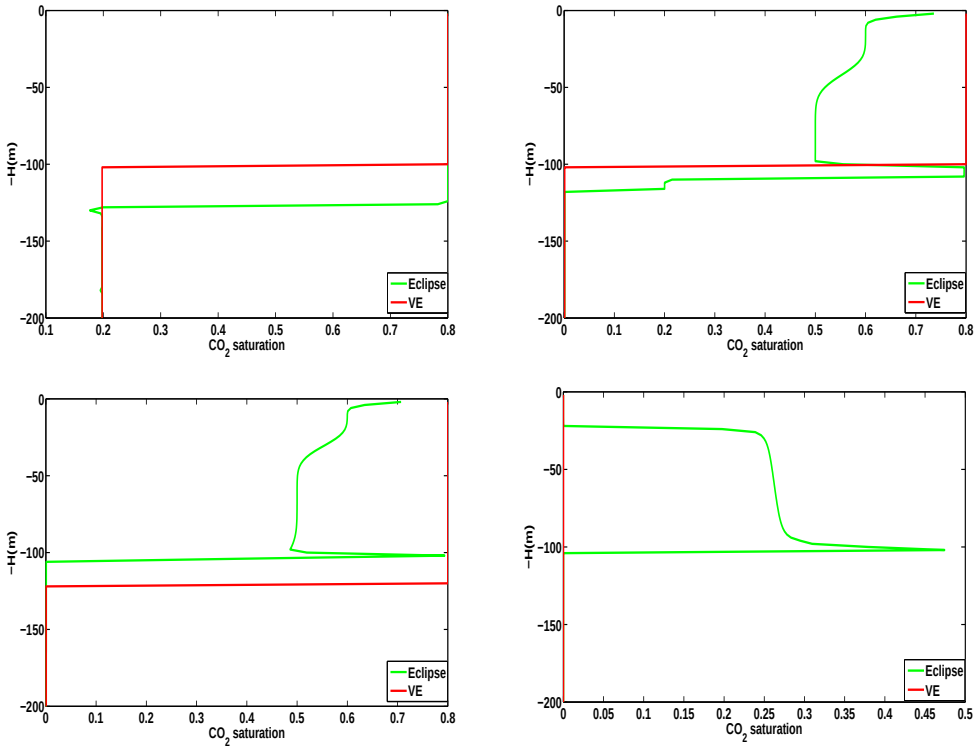

Figure 5.10: Vertical profiles at different x positions after 1500 years for simulation C. First (top left), inside the initial CO_2 saturation, at 6.8 km, second (top right) at 10.8 km, third (bottom left) at 14.4 km and fourth (bottom right) at 16.8 km away from the first edge of the initial CO_2 saturation.

The vertical profiles show the same for simulation B. The sharp interface approximation is not satisfied in this case also. In Figure (5.7 top right) we notice also a small oscillation in the residual CO_2 saturation values. This can be also noticed in the Eclipse simulation Figure (5.8 middle) where there are three cells with CO_2 saturation goes under the residual values which means that we have some numerical errors in Eclipse calculations.

5.1.4 Simulation D

In comparison between simulations B, C and D, the higher permeability in the upper layer the more CO_2 migrated in the vertical direction, the higher CO_2 saturation at the top of the aquifer and the less distance migrated at the top of the lower layer of the aquifer. Figure 5.12 shows that the two solutions start to be closer to each other more than in simulations B and C. This is because of the sharp interface approximation in simulation D is invalid just in a finite region (60.8 km – 62 km), where the vertical shots taken at different positions of the plume shows that clearly, and this is the reason why we still see two different plumes in Figure 5.12. We can also notice that the first edge of the vertically averaged solution is not any more sharp as we have seen in the previous simulations.

Over time, the sharp interface will be valid in any region in this simulation. This can been seen clearly from Figure (5.14 bottom) where the high concentration of CO_2 starts to decrease due to the buoyancy of CO_2 in the vertical direction.

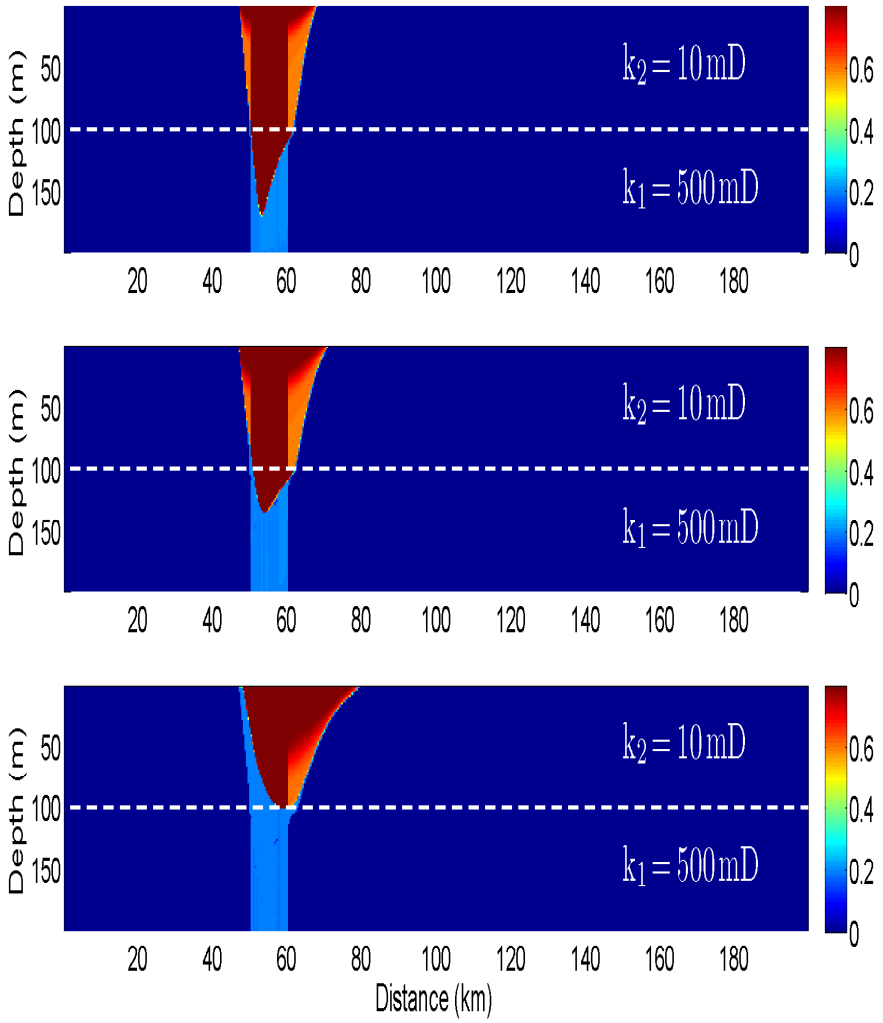

Figure 5.11: Simulation D: simulated CO_2 saturation after 1000 (top), 1500 (middle) and 3000 (bottom) years. Light blue areas indicate immobile CO_2, red areas correspond to mobile CO_2 and dark blue regions indicate pure brine.

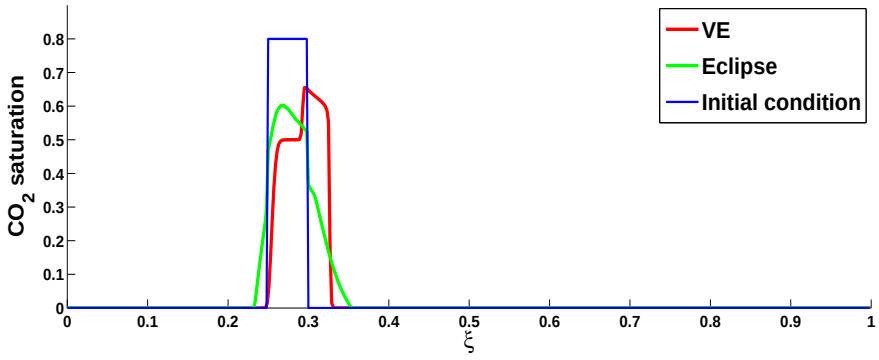

Figure 5.12: Simulation D: vertically averaged saturation values after 1500 years.

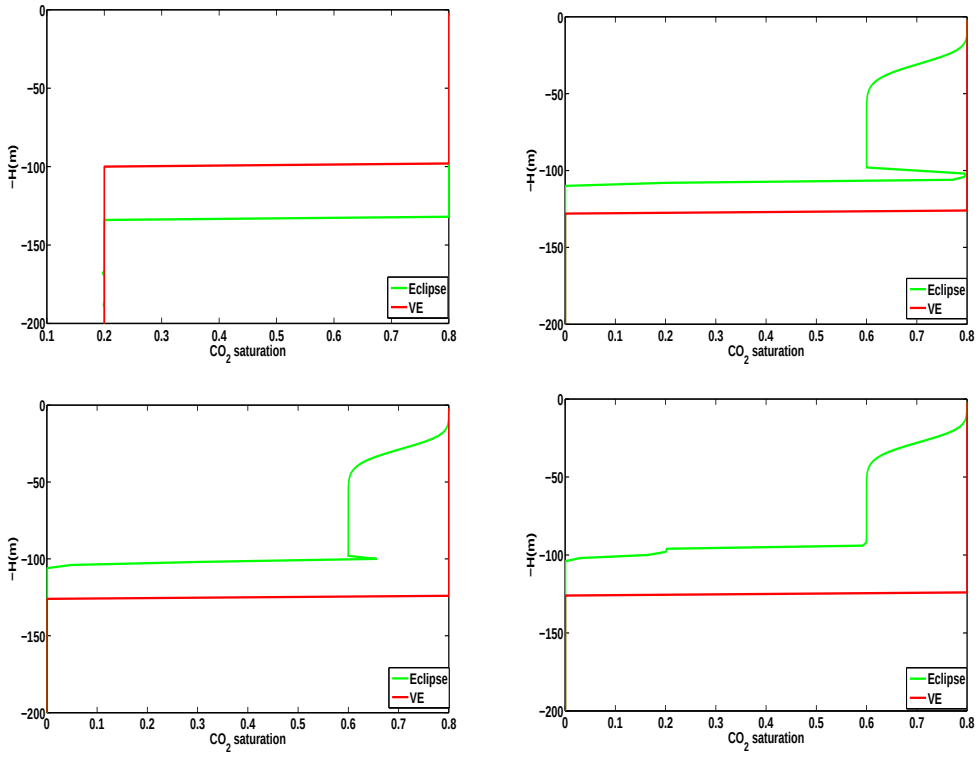

Figure 5.13: Vertical profiles at different x positions after 1500 years for simulation D. First (top left) at 5 km and second (top right) at 10.8 km, third (bottom left) at 12 km and fourth (bottom right) at 12.4 km away from the first edge of the initial CO_2 saturation.

5.1.5 Simulation E

The results of this simulation show that the two solutions becomes closer and closer to each other as we increase the permeability (layer-permeability-ratio) in the the upper layer of the aquifer. The results here show one CO_2 plume in both solutions, and this is because the CO_2 moves in the vertical direction first until it reaches the top of the aquifer then starts moving in the x-direction forming one plume. The way it moves in this simulation is too similar to that in simulation A but with differences in the distance migrated at a specific time and different CO_2 concentration in the grid cells being filled with CO_2.

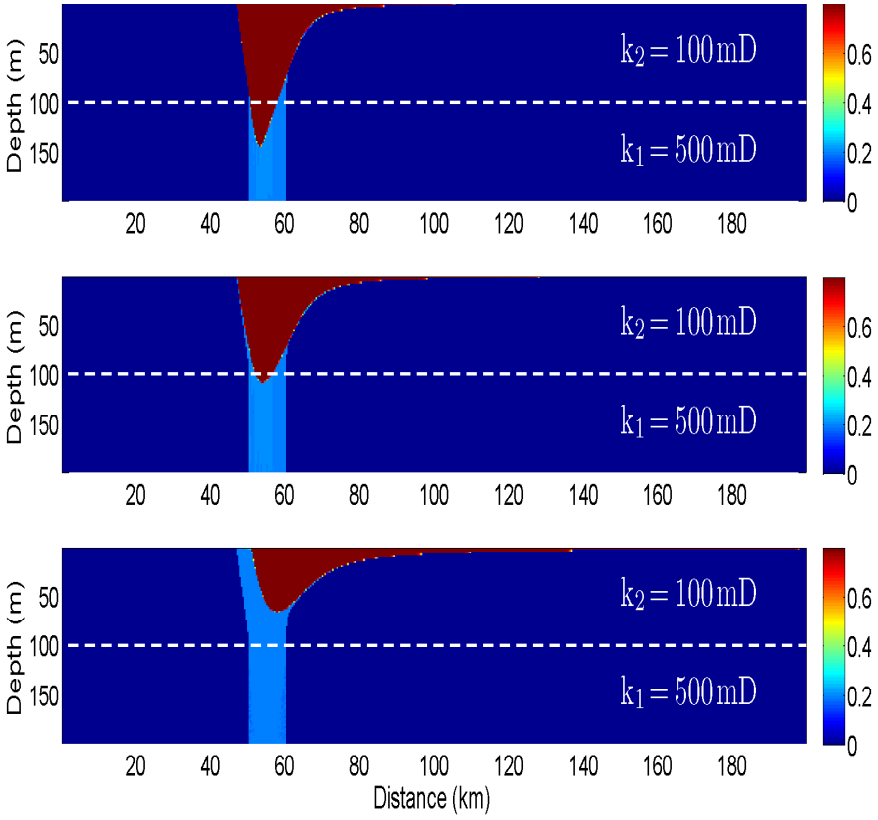

Figure 5.14: Simulation E: simulated CO_2 saturation after 1000 (top), 1500 (middle) and 3000 (bottom) years. Light blue areas indicate immobile CO_2, red areas correspond to mobile CO_2 and dark blue regions indicate pure brine.

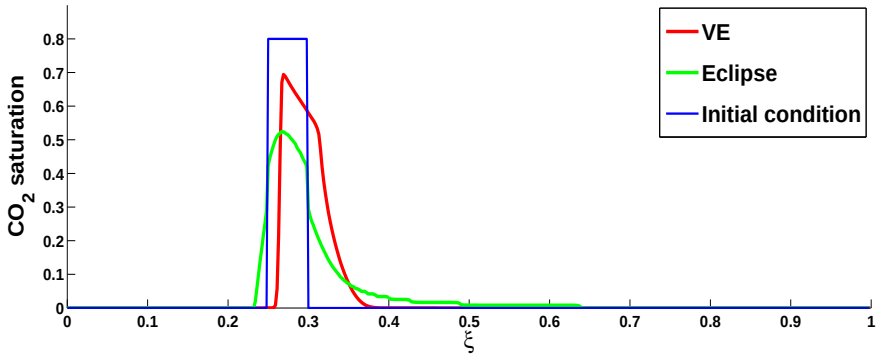

Figure 5.15: Simulation E: vertically averaged saturation values after 1500 years.

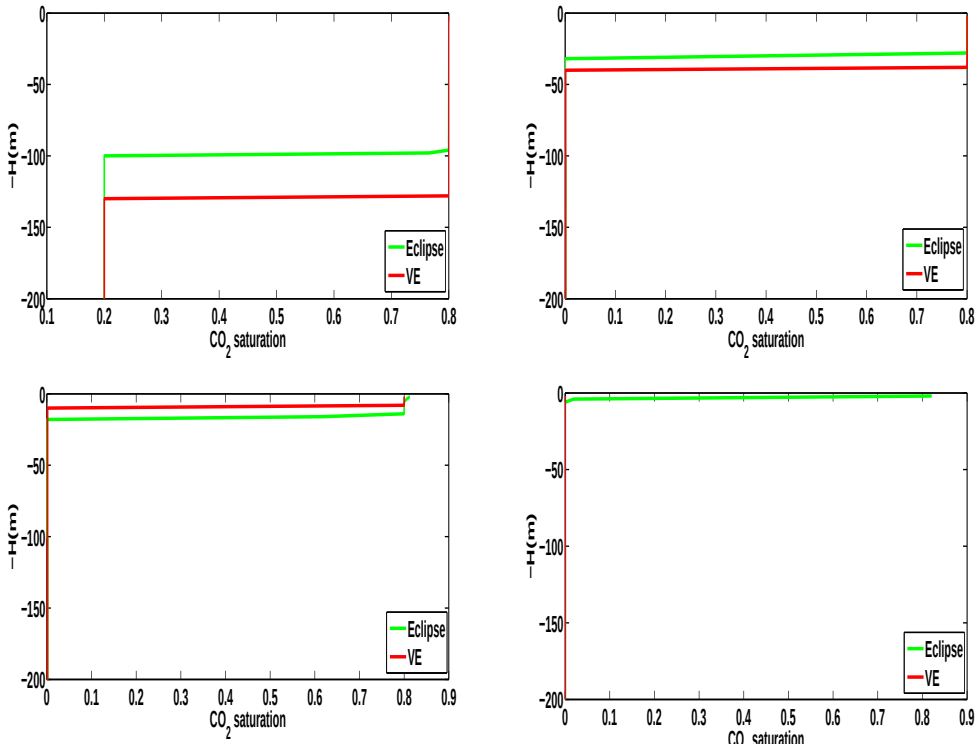

Figure 5.16: Vertical profiles at different positions taken at 1500 years of simulation E. First (top left), inside the initial CO_2 saturation, at 6.7 km, second (top right) at 16.7 km, third (bottom left) at 21.7 km and fourth (bottom right) at 49.2 km away from the first edge of the initial CO_2 saturation.

5.1.6 Distance migrated

Time and distance migrated for all simulations are summarized in Table 5.1, noting that the distance measured at the tip of CO_2 plume at the top of the upper layer except for simulation B where the distance measured at the top of the lower layer, as shown in Figure 5.17.

We recognize that the plume detaches (disconnected from the bottom cap rock) first in simulation E, then in simulations D, C, B and A respectively. The longer distance migrated is in simulation A, E, B, D and D respectively, noting that in simulation A, B and E the tip of the plume is very thin and covers a very long distance, while in simulation C and D the plume tip is thick due to the permeability difference in the upper layer of the aquifer. High (100 mD) and very low (0.1 mD) permeability values of k_2 gives longer migrated distance and thinner plume tip at the top of the upper layer and lower layer respectively, while the intermediate (1 and 10 mD) values gives shorter distance and thicker plume tip at the top of the upper layer.

	Time in years			CO_2 plume detaches	
	1000	1500	3000	Distance	Time(year)
Simulation A	72.4 km	109.2 km	138.4 km	76 km	1050
Simulation B	32 km	36 km	38.8 km	30.8 km	900
Simulation C	5.6 km	8 km	11.2 km	5.6 km	765
Simulation D	8 km	10.8 km	19.2 km	6.4 km	700
Simulation E	45.6 km	68 km	137.6 km	26.8 km	580

Table 5.1: Distance traveled by the plume at different times. Distance is measured from the second edge of the initial CO_2 plume. In simulation B, the distance is measured in the lower layer.

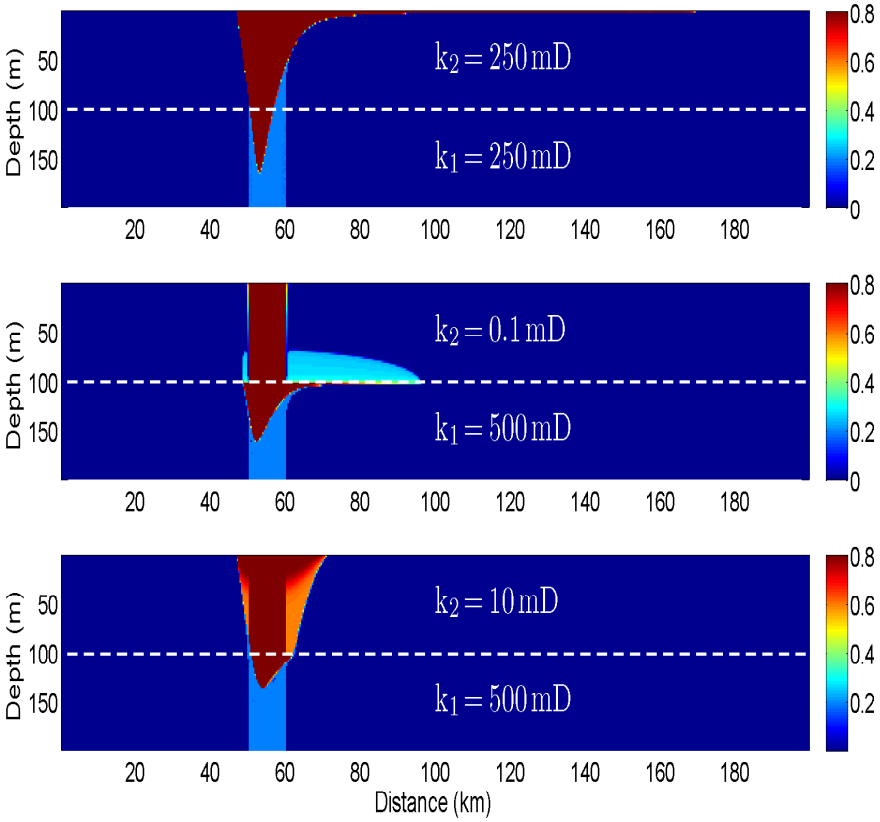

Figure 5.17: Distance migrated in different simulations at 1500 years, simulation A (top), simulation B (middle) and simulation D (bottom).

5.2 Height effect

Here we will investigate the effect of the height (h) of the upper (low permeability) and lower (high permeability) layer of the initial conditions on the CO_2 plume evolution, upon decreasing the first and increasing the second height. Two cases are being considered here, $h_{upper} = \frac{1}{4}H$ and $h_{upper} = \frac{1}{8}H$.

5.2.1 Simulation B

Figure 5.18 shows CO_2 saturations distribution after 1500 years. We observe that we are still having two different solutions in both cases as simulation B in the reference case, where the sharp interface approximation clearly fails. The highest CO_2 concentrations are located at the top of the lower layer of the aquifer in the advection part, where some CO_2 starts migrating upward without reaching the top of the aquifer ($h = \frac{1}{4}H$). When it reaches the top of the aquifer ($h = \frac{1}{8}H$) the concentrations start to increase from the top down to the lower edge of the upper layer of the aquifer.

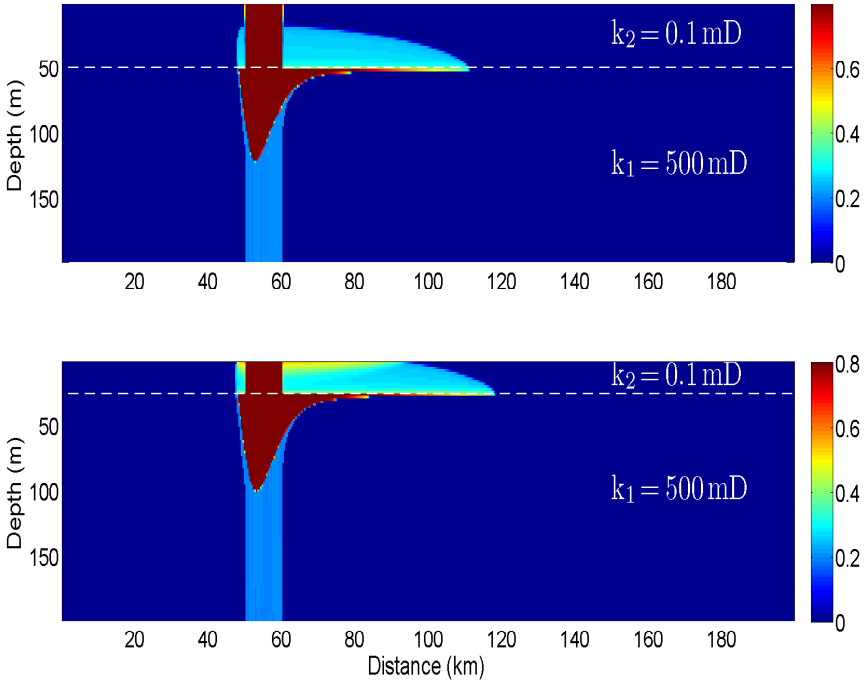

Figure 5.18: Simulation B: Eclipse simulation after 1500 years, for $h = \frac{1}{4}H$ (top) and for $h = \frac{1}{8}H$ (bottom).

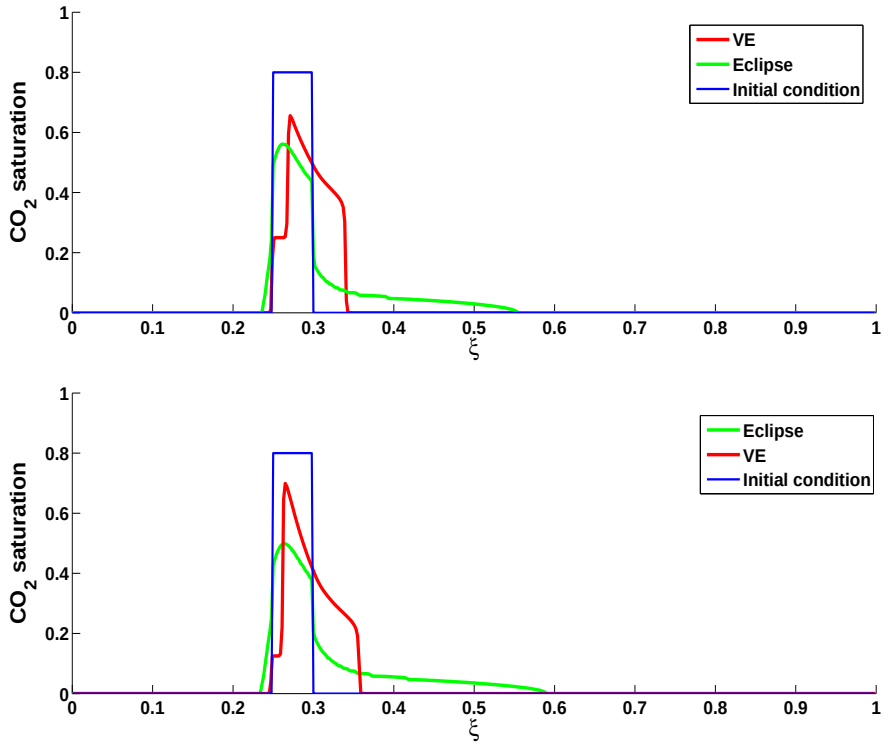

Figure 5.19: Simulation B: VE solution after 1500 years, for $h = \frac{1}{4}H$ (top) and for $h = \frac{1}{8}H$ (bottom).

5.2.2 Simulation C

We observe the same movement behavior of CO_2 as in simulation B above, but this time more CO_2 has migrated upwards and become more concentrated at the top of the upper layer because of the higher permeability. We can expect this result at simulation B over time. The difference in this case will be the distance migrated in both cases at the top of the lower layer.

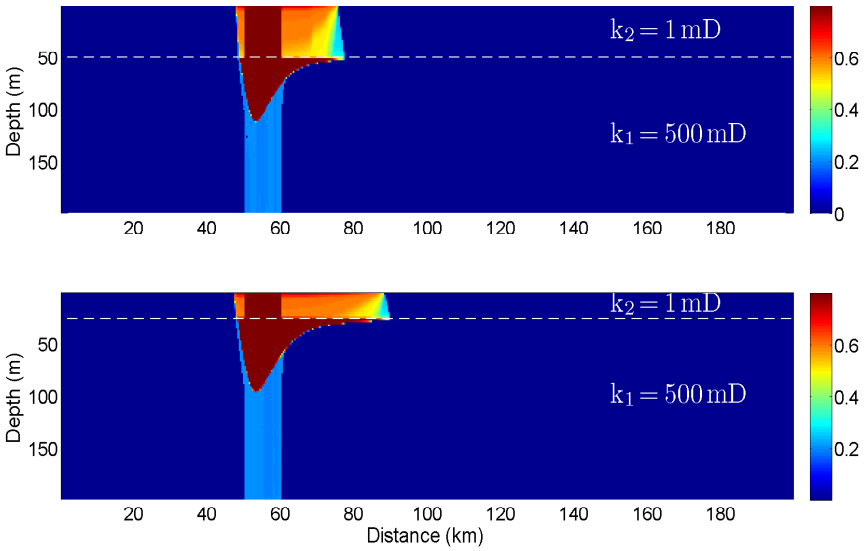

Figure 5.20: Simulation C: Eclipse simulation after 1500 years, for $h = \frac{1}{4}H$ (top) and for $h = \frac{1}{8}H$ (bottom).

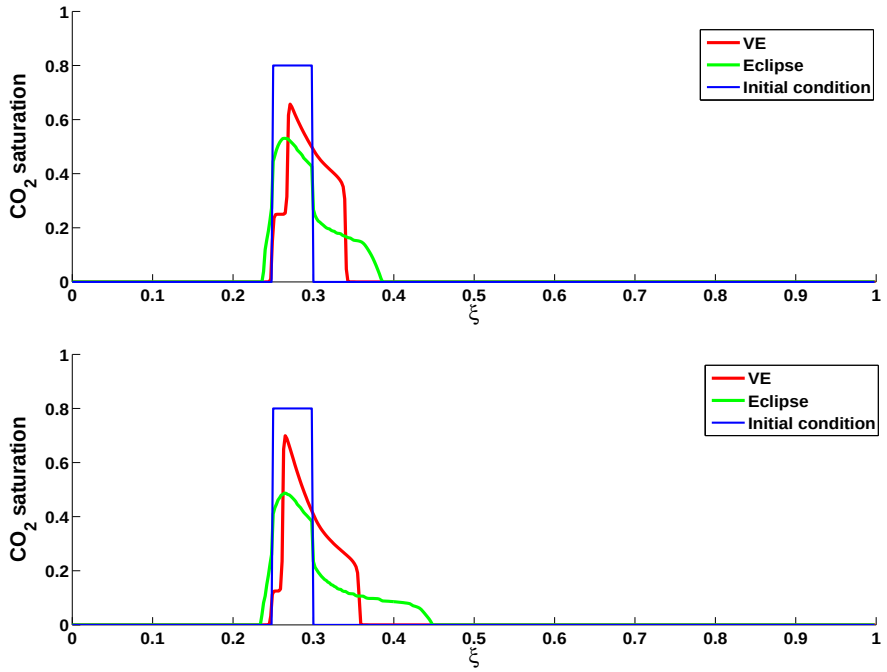

Figure 5.21: Simulation C: VE solution after 1500 years, for $h = \frac{1}{4}H$ (top) and for $h = \frac{1}{8}H$ (bottom).

5.2.3 Simulation D

This simulation produces the same behavior of CO_2 as in simulation C, with more CO_2 concentration at the top of the aquifer and less distance migrated.

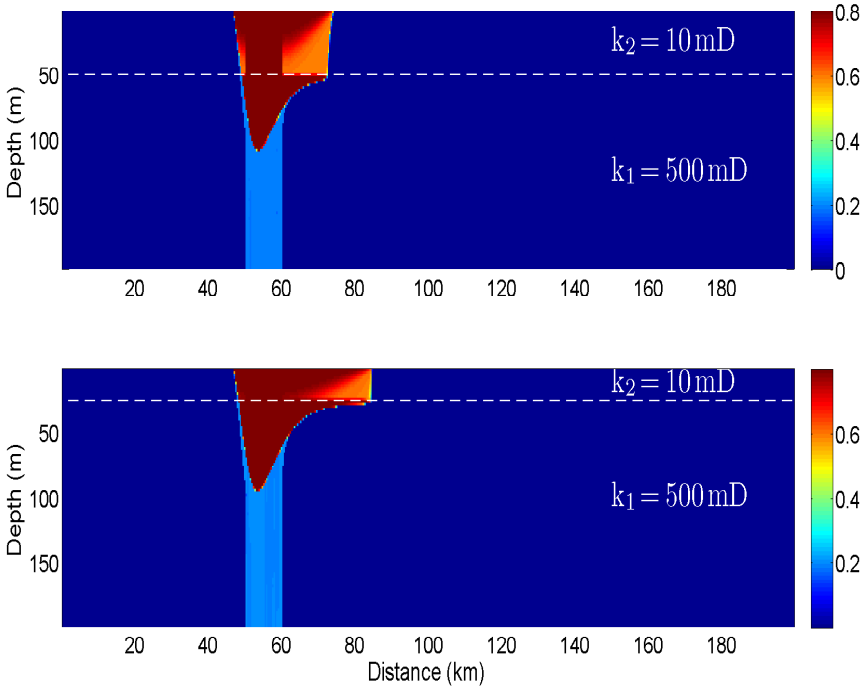

Figure 5.22: Simulation D: Eclipse simulation after 1500 years, for $h = \frac{1}{4}H$ (top) and for $h = \frac{1}{8}H$ (bottom).

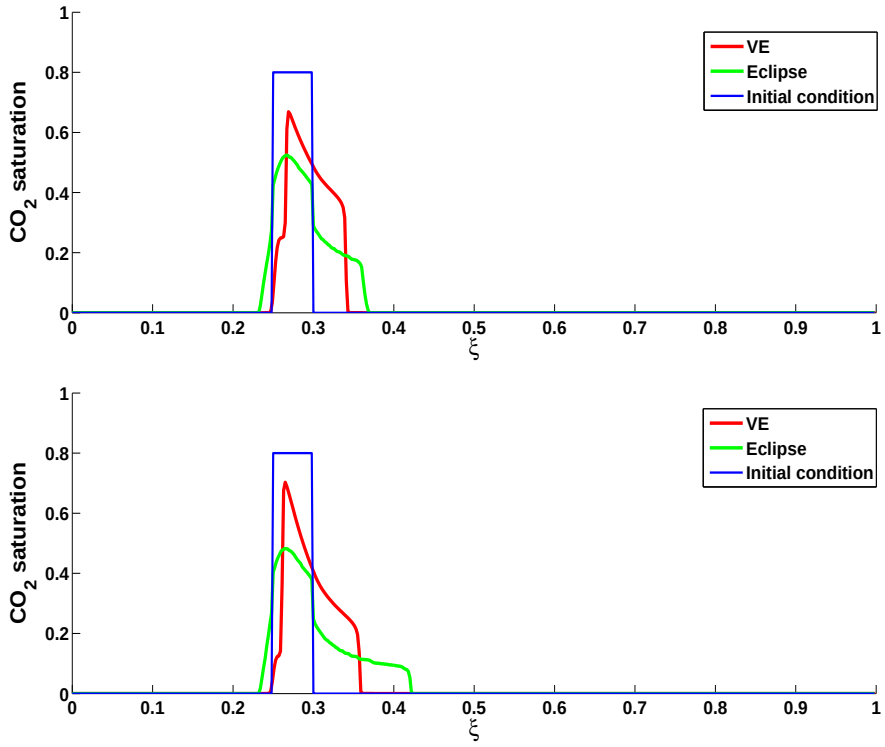

Figure 5.23: Simulation D: VE solution after 1500 years, for $h = \frac{1}{4}H$ (top) and for $h = \frac{1}{8}H$ (bottom).

5.2.4 Simulation E

This simulation also produces the same CO_2 behavior as before, but here the Eclipse simulation in Figure 5.24 shows one CO_2 plume migrating with a pre-elongated tongue in the advection part. The VE solution is shown in Figure 5.25.

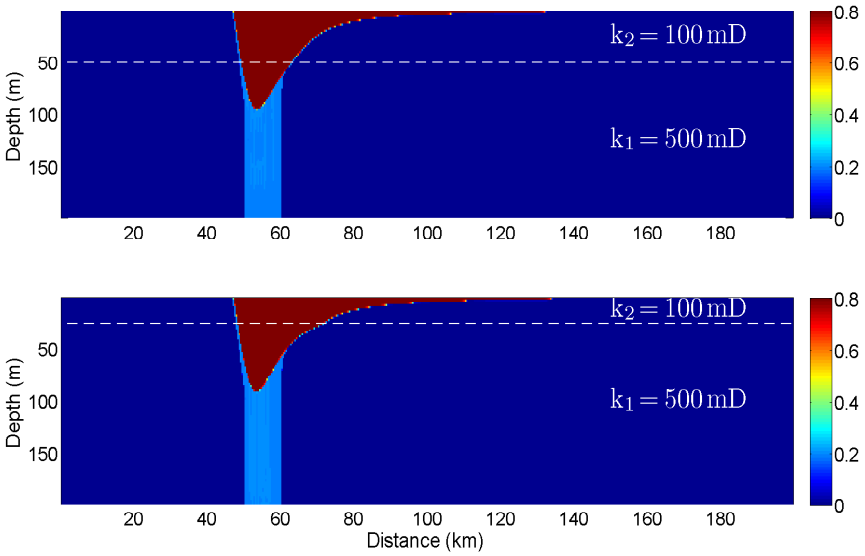

Figure 5.24: Simulation E: Eclipse simulation after 1500 years, for $h = \frac{1}{4}H$ (top) and for $h = \frac{1}{8}H$ (bottom).

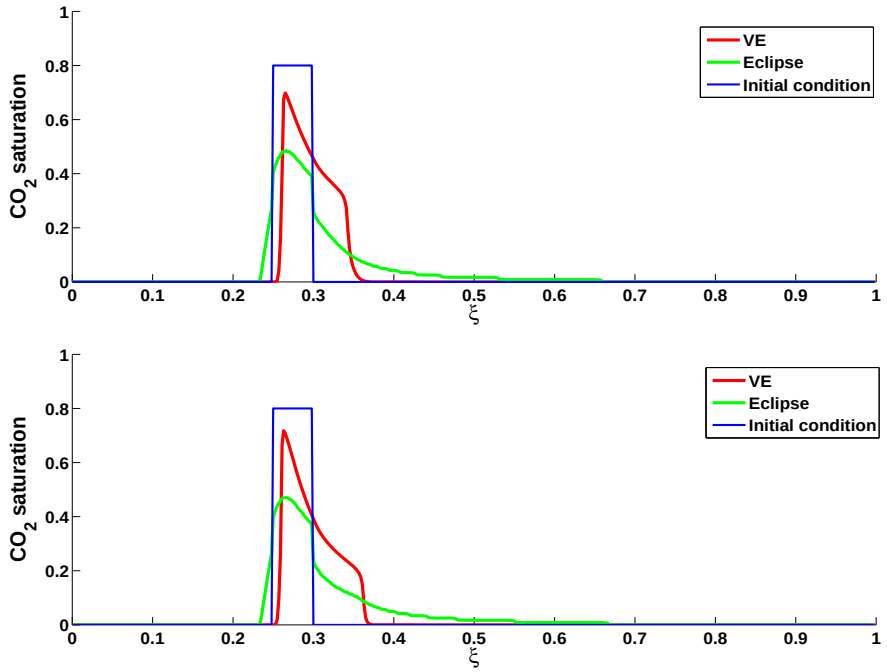

Figure 5.25: Simulation E: VE solution after 1500 years, for $h = \frac{1}{4}H$ (top) and for $h = \frac{1}{8}H$ (bottom).

5.2.5 Distance migrated

Comparing the results together, we find that the longest distances migrated by the plume are in simulation E and the shortest distances are in simulation D.

Distance migrated after 1500 years in the previous simulations with different heights of the upper lower permeability layer is summarized as

	At 1500 years		
	h=$\frac{1}{2}$H	h=$\frac{1}{4}$H	h=$\frac{1}{8}$H
Simulation B	36 km	51.2 km	58 km
Simulation C	8 km	17.2 km	30 km
Simulation D	10.8 km	14 km	24.4 km
Simulation E	68 km	72 km	73.6 km

Table 5.2: Distance measured from the second edge of the initial CO_2 plume.

	CO_2 plume detaches			
	h=$\frac{1}{4}$H		h=$\frac{1}{8}$H	
	Time(years)	Distance	Time(years)	Distance
Simulation B	695	36.8 km	595	38 km
Simulation C	640	10.8 km	595	15.6 km
Simulation D	600	7.2 km	565	11.2 km
Simulation E	565	27.6 km	550	27.6 km

Table 5.3: Time and distance migrated when the CO_2 plume detaches from the lower cap rock.

5.3 Permeability-layer-ratio inverse effect

For the simulations above, the lpermeability-layer-ratio was k_2/k_1 which corresponds to B_2/B_1, C_2/C_1, D_2/D_1 and E_2/E_1in the fractional flow figure. Now, switching the permeability values between the two layers into k_1/k_2 which corresponds to B_1/B_2, C_1/C_2, D_1/D_2 and E_1/E_2, in order to study the effect of the permeability order.

First, we present the fractional flow functions for these simulations in Figure 5.26, where we observe that the fractional flow functions in the two-layer aquifer is continuous for all simulation scenarios, where the solid and dashed lines represent the fractional flow function in the upper layer and lower layer of the aquifer, respectively. It also shows that the sonic point always exists when the CO_2 plume is in upper layer of the aquifer.

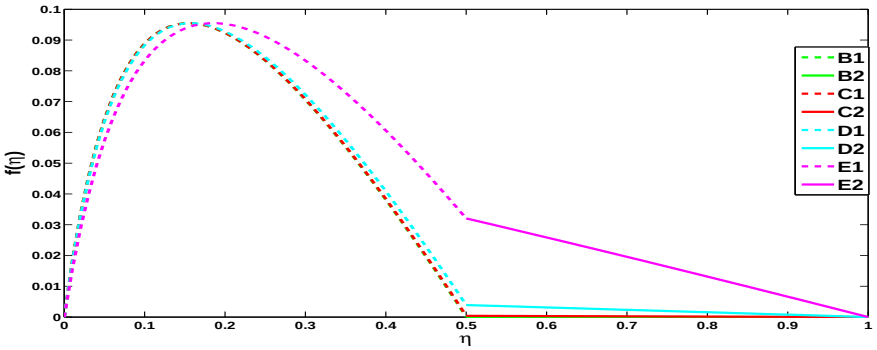

Figure 5.26: Fractional flow function for the switched permeability values.

5.3.1 Simulation B and C

In both simulations we are restricted in presenting the Eclipse simulations after 500 years only, because the simulation does not converge ($S_{nw} > 0.8$) any more after that time. The divergence of these simulations is due to i) numerical errors in Eclipse simulator and/ or ii) model we present.

Simulation B

An interesting result from Eclipse simulation shows that we have two separated plumes. The first plume migrating in the upper layer under the same behavior as the homogeneous case, where a very small volume of the second plume in the lower layer very slightly migrated in the upward direction.

Simulation C

The same image has been noticed as in simulation B with much more CO_2 of the second plume migrated in the vertical direction.

The two separated plumes in simulation C do not hold for a long time before the second plume joins the first due to the permeability value in the lower layer, while this result hold for a much longer time due to the poor permeability value in the lower layer.

In both simulation during imbibition, first the brine displaces CO_2 in the horizontal direction in the upper layer producing the cone shape of the CO_2 that is connected to the top cap rock, then displaces CO_2 in the vertical

direction in the lower layer producing the cone shape connected to the bottom cap rock. See Figure 5.27

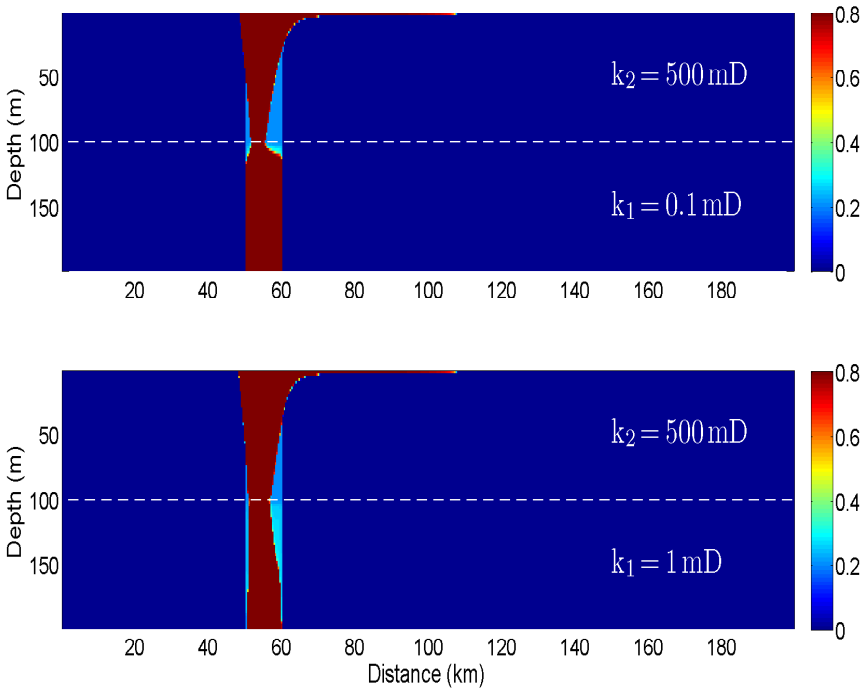

Figure 5.27: Eclipse simulation results after 500 years for simulation B (top) and simulation C (bottom).

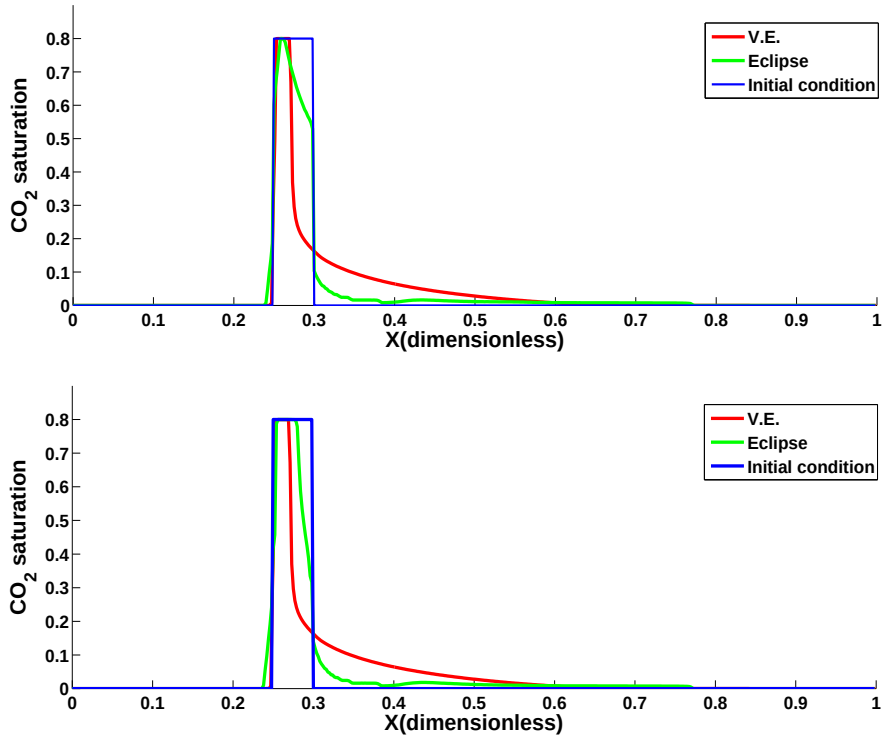

Figure 5.28: VE solution after 500 years for simulation B (top) and simulation C (bottom).

5.3.2 Simulation D

The solutions here are "almost" the same for the lower layer of the aquifer with a small shift of approximately 3 meters. The sharp interface approximation fails only in the grid columns where CO_2 migrates upward as shown in the Eclipse results. A comparison of the results with that found in the reference case simulation E, shows that the inverse ratio plays a very important role in the plume shape and distance migrated.

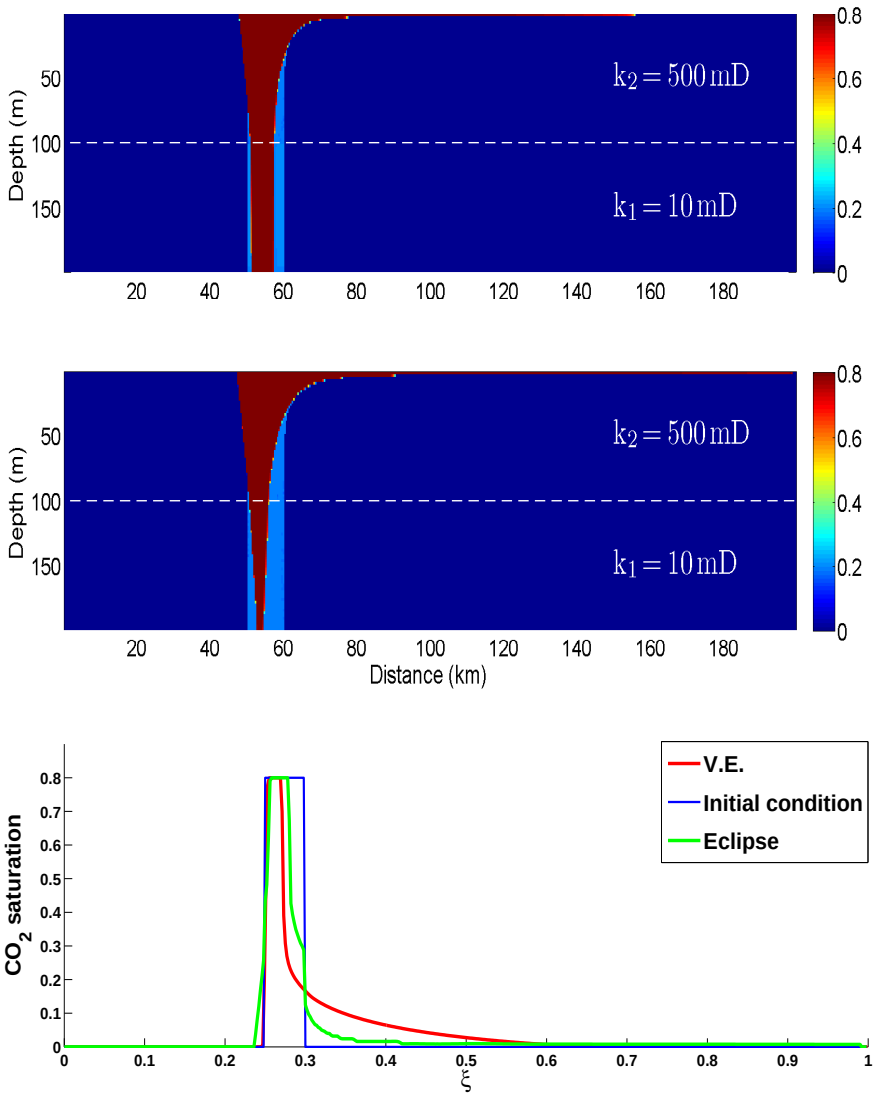

Figure 5.29: Simulation D: Eclipse simulation at 1000 (top), at 1500 (middle) years and Eclipse and VE solution after 1500 (bottom) years.

5.3.3 Simulation E

In this case, the sharp interface holds all the time and the results show exactly the same solution for the lower layer of the aquifer. The solution

here follows the same behavior as the previous simulation with differences in the distribution of CO_2 saturation and amount migrated due to the higher permeability in the lower layer.

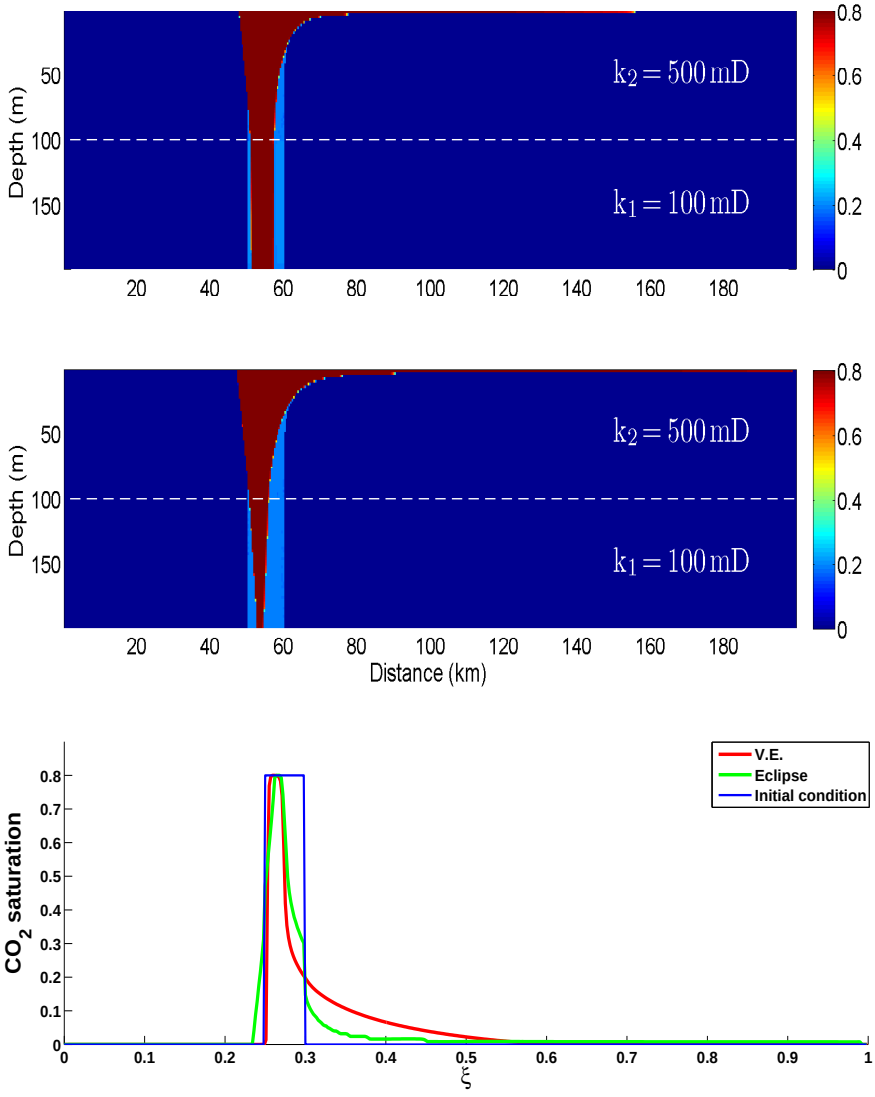

Figure 5.30: Simulation E: Eclipse simulation at 1000 (top), at 1500 (middle) years and Eclipse and VE solution after 1500 (bottom) years.

5.3.4 Distance migrated

In both simulations B and C the distance migrated by both plumes is 94 km. A near distance migrated in both simulation were expected because the only difference between both is that more CO_2 migrated upwards from the second plume, but this volume plays a role in the CO_2 saturations in the advection part where it has been noticed there is more concentration of CO_2 .

In both simulations D and E, the CO_2 reaches the end of the aquifer where we have cells with much higher volume capacity. So this means that the plume could have migrated more than this if we had a longer distance. The remarkable result in simulation D is that after 3125 years of simulation the CO_2 plume did not detach with a thickness of 1.6 km in the x-direction connected to the bottom of the aquifer, while in simulation E the plume detached after 1960 years.

Chapter 6

Conclusion

We have derived a vertical-equilibrium (VE) sharp-interface model describing the migration of CO_2 plume with residual trapping in a tilted aquifer with N horizontal permeability layers. We used this model to study the effect of heterogeneity on the shape and distance migrated by the CO_2 plume. The VE model (horizontal flow only) produced robust results in the sense of being physically meaningful in all our simulations. However, in some of the cases simulated, the VE-results differed significantly from results obtained from Eclipse simulations. Furthermore, we believe that the Eclipse-simulations are closer to the exact solutions to the problems we have investigated in this thesis.

The results show that the two permeability layers have a significant impact on the shape of CO_2 plume and migrating distance depending on the layer-permeability-ratio, k_2/k_1. When the upper layer is less permeable than the lower layer ($k_2/k_1 \ll 1$), we found that two CO_2 plumes developed.

At early time, we notice that the sharp interface approximation fails in the two-permeability-layer aquifer. At very late time we expect that the sharp interface approximation will hold. This is because the whole CO_2 plume migrates upwards into the upper layer and migrate further below the no flow cap rock as in the homogeneous case.

We also studied the effect of the height of the upper and lower layer on the CO_2 plume shape and distance migrated when $k_2/k_1 \ll 1$. The smaller height of the upper layer leads to more mobile CO_2 volume within the high permeability layer. This results in longer migrated distance in the top of the lower layer (at the top of the aquifer for the simulation E, $k_2/k_1 = 5$) and higher CO_2 saturations on the top of the aquifer. The height of the upper layer plays an important role in the evolution of the CO_2 plume by

shortening the time during which the sharp interface approximation fails. In real reservoirs during and after injection, we expect a smaller amount of CO_2 in a low permeability region than that in a higher permeability region.

Moreover, we studied the effect of the inverse of the permeability-layer-ratio ($k_2/k_1 \gg 1$). We observed that the initial plume evolves such that two separated CO_2 plumes form in simulation B ($k_2/k_1 = 5000$) and C ($k_2/k_1 = 500$). In these two simulations, during imbibition the brine displaces CO_2 in the horizontal direction (brine moves from right to left side) in the upper layer while it displaces the CO_2 in the vertical direction (brine moves from top to bottom) in the lower layer. This poses a question about the VE model. Over time, the lower plume in simulation C ($k_2/k_1 = 500$) will connect again with the upper plume much faster than that in simulation B ($k_2/k_1 = 5000$) due to the very poor permeability in the lower layer of aquifer, where it is too difficult for the CO_2 to move upwards.

These results suggest that we have to be more careful when we derive the mathematical model under the sharp interface approximation, where it fails in most of our simulation results. When the VE and Eclipse simulation results do not agree, this could be because i) VE is not achieved (the basic assumption of VE is not satisfied) and/or ii) the fine scale reconstruction of the VE solution is wrong. If VE is not achieved, then it is important to consider the vertical flow where the vertical velocity of the flow is not any more small ($k_2/k_1 = 5000$ and $k_2/k_1 = 500$). If reconstruction is wrong, then more effort should be put on that part to balance the effect of simplifications assumed before.

Bibliography

[1] CO_2 capture project. http://www.co2captureproject.org/CO_2trapping.html, downloaded on May 14, 2010.

[2] M.A. Celia, S. Bachu, J.M. Nordbotten, S.E. Gasda, and H.K. Dahle. Quantitative estimation of CO_2 leakage from geological storage: Analytical models, numerical models and data needs. pages 5–9, 2004.

[3] FAL Dullien. *Porous media; fluid transport and pore structure*. Academic press, 1979.

[4] S.M. Frailey and H. Leetaru. Geological factors affecting co2 plume distribution. *Energy Procedia*, 1(1):3107–3112, 2009.

[5] M.R. Gadallah and R.L. Fisher. *Applied seismology: a comprehensive guide to seismic theory and application*. 2005.

[6] S.E. Gasda, J.M. Nordbotten, and M.A. Celia. Vertical equilibrium with sub-scale analytical methods for geological CO_2 sequestration. *Computational Geosciences*, 13(4):469–481, 2009.

[7] S. Geoquest. *FILL Reference Manual*, 2006.1.

[8] S. Geoquest. *ECLIPSE Reference Manual*, 2007.1.

[9] Andreas Hammer. Vertically averaged models for CO_2 storage in porous media. Master's thesis, University of Bergen, Nov 2008.

[10] M.A. Hesse, FM Orr, and HA Tchelepi. Gravity currents with residual trapping. *Journal of Fluid Mechanics*, 611:35–60, 2008.

[11] M.A. Hesse, H.A. Tchelepi, B.J. Cantwel, and F.M. Orr. Gravity currents in horizontal porous layers: transition from early to late self-similarity. *Journal of Fluid Mechanics*, 577:363–383, 2007.

[12] J.M. Nordbotten K. Pruess H.K. Dahle, G.T. Eigestad. A model-oriented benchmark problem for CO_2 storage. August 2009.

[13] S. Holloway and D. Savage. The potential for aquifer disposal of carbon dioxide in the UK. *Energy Conversion and Management*, 34(9-11):925–932, 1993.

[14] R. Juanes, C.W. MacMinn, and M.L. Szulczewski. The footprint of the CO_2 plume during carbon dioxide storage in saline aquifers: Storage efficiency for capillary trapping at the basin scale. *Transport in Porous Media*, pages 1–12, 2009.

[15] R. Juanes, E.J. Spiteri, F.M. Orr Jr., and M.J. Blunt. Impact of relative permeability hysteresis on geological CO_2 storage. *Water Resour. Res*, 42:W12418, 2006.

[16] R.J. LeVeque. *Numerical methods for conservation laws*. Birkh "a user, 1992.

[17] B. Metz. *IPCC special report on carbon dioxide capture and storage*. Cambridge University Press, 2005.

[18] B. Metz, O. Davidson, H. Coninck, et al. Carbon dioxide capture and storage. special report, intergovernmental panel on climate change. 2005.

[19] J.M. Moschetta and J. Gressier. The sonic point glitch problem: A numerical solution. In *Sixteenth International Conference on Numerical Methods in Fluid Dynamics*, pages 403–408. Springer, 1998.

[20] J.A. Neufeld and H.E. Huppert. Modelling carbon dioxide sequestration in layered strata. *Journal of Fluid Mechanics*, 625:353–370, 2009.

[21] D.A. Nield and A. Bejan. *Convection in porous media*. Springer Verlag, 2006.

[22] Jan Martin Nordbotten. *Sequestration of Carbon in Saline Aquifers*. PhD thesis, Dep. Of Math., University of Bergen., 2004.

[23] J.M. Nordbotten, M.A. Celia, and S. Bachu. Injection and storage of CO_2 in deep saline aquifers: Analytical solution for CO_2 plume evolution during injection. *Transport in Porous Media*, 58(3):339–360, 2005.

[24] J.M. Nordbotten and H. K. Dahle. Impact of the capillary fringe in vertically integrated models for CO_2 storage. 2009.

[25] J.M. Nordbotten and Pruess Kartsen. Numerical simulation studies of the long-term evolution of a CO_2 plume in a saline aquifer with a sloping caprock. 2009.

[26] N. RILEY. *Geological Storage of Carbon Dioxide*. Royal Society of Chemistry, 2009.

[27] Renate von der Ohe. A godunov base operator splitting method for a system of convection-diffusion equations. Master's thesis, University of Bergen, 1999.

[28] Y.C. Yortsos. A theoretical analysis of vertical flow equilibrium. *Transport in Porous Media*, 18(2):107–129, 1995.

[29] Øystein Pettersen. Basics of reservoir simulation with the eclipse reservoir simulator. 2006.